








ARTICLE

<https://doi.org/10.1038/s41467-019-09276-w>

OPEN

Rbpj expression in regulatory T cells is critical for restraining T_H2 responses

Michael Delacher ^{1,2,3}, Christian Schmidl ², Yonatan Herzig⁴, Minka Breloer ⁵, Wiebke Hartmann⁵, Fabian Brunk⁶, Danny Kägebein³, Ulrike Träger³, Ann-Cathrin Hofer³, Sebastian Bittner^{1,2}, Dieter Weichenhan⁷, Charles D. Imbusch ⁸, Agnes Hotz-Wagenblatt⁹, Thomas Hielscher¹⁰, Achim Breiling ¹¹, Giuseppina Federico¹², Hermann-Josef Gröne¹², Roland M. Schmid¹³, Michael Rehli ^{2,14}, Jakub Abramson⁴ & Markus Feuerer ^{1,2,3}

The transcriptional regulator Rbpj is involved in T-helper (T_H) subset polarization, but its function in T_{reg} cells remains unclear. Here we show that T_{reg}-specific Rbpj deletion leads to splenomegaly and lymphadenopathy despite increased numbers of T_{reg} cells with a polyclonal TCR repertoire. A specific defect of Rbpj-deficient T_{reg} cells in controlling T_H2 polarization and B cell responses is observed, leading to the spontaneous formation of germinal centers and a T_H2-associated immunoglobulin class switch. The observed phenotype is environment-dependent and can be induced by infection with parasitic nematodes. Rbpj-deficient T_{reg} cells adopt open chromatin landscapes and gene expression profiles reminiscent of tissue-derived T_H2-polarized T_{reg} cells, with a prevailing signature of the transcription factor Gata-3. Taken together, our study suggests that T_{reg} cells require Rbpj to specifically restrain T_H2 responses, including their own excessive T_H2-like differentiation potential.

¹Chair for Immunology, University Regensburg and University Hospital Regensburg, Franz-Josef-Strauss-Allee 11, 93053 Regensburg, Germany. ²Regensburg Center for Interventional Immunology (RCI), University Regensburg and University Hospital Regensburg, Franz-Josef-Strauss-Allee 11, 93053 Regensburg, Germany. ³Immune Tolerance Group, Tumor Immunology Program, German Cancer Research Center (DKFZ), Im Neuenheimer Feld 280, 69120 Heidelberg, Germany. ⁴Department of Immunology, Weizmann Institute of Science, 234 Herzl Street, 76100 Rehovot, Israel. ⁵Bernhard Nocht Institute for Tropical Medicine, Bernhard-Nocht-Straße 74, 20359 Hamburg, Germany. ⁶Division of Developmental Immunology, German Cancer Research Center (DKFZ), Im Neuenheimer Feld 280, 69120 Heidelberg, Germany. ⁷Division of Epigenomics and Cancer Risk Factors, German Cancer Research Center (DKFZ), Im Neuenheimer Feld 280, 69120 Heidelberg, Germany. ⁸Division of Applied Bioinformatics, German Cancer Research Center (DKFZ), Im Neuenheimer Feld 280, 69120 Heidelberg, Germany. ⁹Genomics and Proteomics Core Facility, German Cancer Research Center (DKFZ), Im Neuenheimer Feld 280, 69120 Heidelberg, Germany. ¹⁰Division of Biostatistics, German Cancer Research Center (DKFZ), Im Neuenheimer Feld 280, 69120 Heidelberg, Germany. ¹¹Division of Epigenetics, German Cancer Research Center (DKFZ), Im Neuenheimer Feld 280, 69120 Heidelberg, Germany. ¹²Division of Cellular and Molecular Pathology, German Cancer Research Center (DKFZ), Im Neuenheimer Feld 280, 69120 Heidelberg, Germany. ¹³Department of Internal Medicine, Technical University of Munich, Ismaninger Straße 22, 81675 Munich, Germany. ¹⁴Department of Internal Medicine III, Hematology and Oncology, University Hospital Regensburg, Franz-Josef-Strauss-Allee 11, 93053 Regensburg, Germany. Correspondence and requests for materials should be addressed to M.F. (email: markus.feuerer@ukr.de)

Regulatory T cells (T_{reg}) are important mediators of peripheral tolerance, and their absence leads to catastrophic autoimmunity in men (IPEX¹) and mice (Scurfy²). T_{reg} cells are characterized by both expression of the hallmark transcription regulator Foxp3^{3–5} and a unique epigenetic profile^{6–9}. T_{reg} cells specialize to fulfill their diverse regulatory functions¹⁰. They can engage defined molecular pathways to specifically suppress either T_H1 -polarized, T_H2 -polarized, or T_H17 -polarized immune effector cells¹¹. For instance, under T_H1 conditions, T_{reg} cells up-regulate expression of the T_H1 -specific transcription factor T-box 21 (T-bet) and accumulate at inflammatory sites¹². Correspondingly, under T_H2 conditions, T_{reg} cells express Gata-binding protein 3 (Gata-3) and interferon regulatory factor 4 (Irf4), and T_{reg} -specific IRF4-deletion leads to IL-4 cytokine production of effector T cells and lymphoproliferative disease¹³. Up-regulation of signal transducer of activated T cells 3 (Stat3) is critical for the capacity of T_{reg} cells to control T_H17 -mediated inflammation, while its T_{reg} -specific deletion results in enhanced IL-17 production by effector cells and intestinal inflammation¹⁴. Therefore, T_{reg} cells integrate unique parts of T_H subtype-specific transcriptional programs to specifically control the respective T_H -polarized immune response.

Recombination signal-binding protein for immunoglobulin kappa J region (Rbpj) is a transcription factor commonly known for its function as a co-factor during Notch signaling, translating extracellular signals into gene expression changes¹⁵. In the context of T cell differentiation and function, Rbpj has been associated with T_H1/T_H2 cell fate decisions^{16,17}. Indeed, in $CD4^+Foxp3^-$ conventional T (T_{conv}) cells, Rbpj in a complex with the Notch intracellular domain (NICD) was shown to be critical for regulation of Gata-3, an important molecular switch for optimal T_H2 responses^{18,19}. In contrast to this, forced expression of the NICD in T_{reg} cells rendered them incapable of suppressing T effector cells and caused autoimmunity²⁰. This indicates that, based on the cellular context, Rbpj and Notch have a different impact on cellular responses. While the importance of Rbpj is well documented in T_H2 subset polarization, its function in T_{reg} cells remains unclear.

Here we unveil a previously unappreciated role of Rbpj in regulating the capacity of T_{reg} cells to restrain T_H2 responses. Loss of Rbpj renders T_{reg} cells more sensitive to T_H2 -inducing conditions and fosters the extensive generation of Gata-3-positive tissue-type T_{reg} cells.

Results

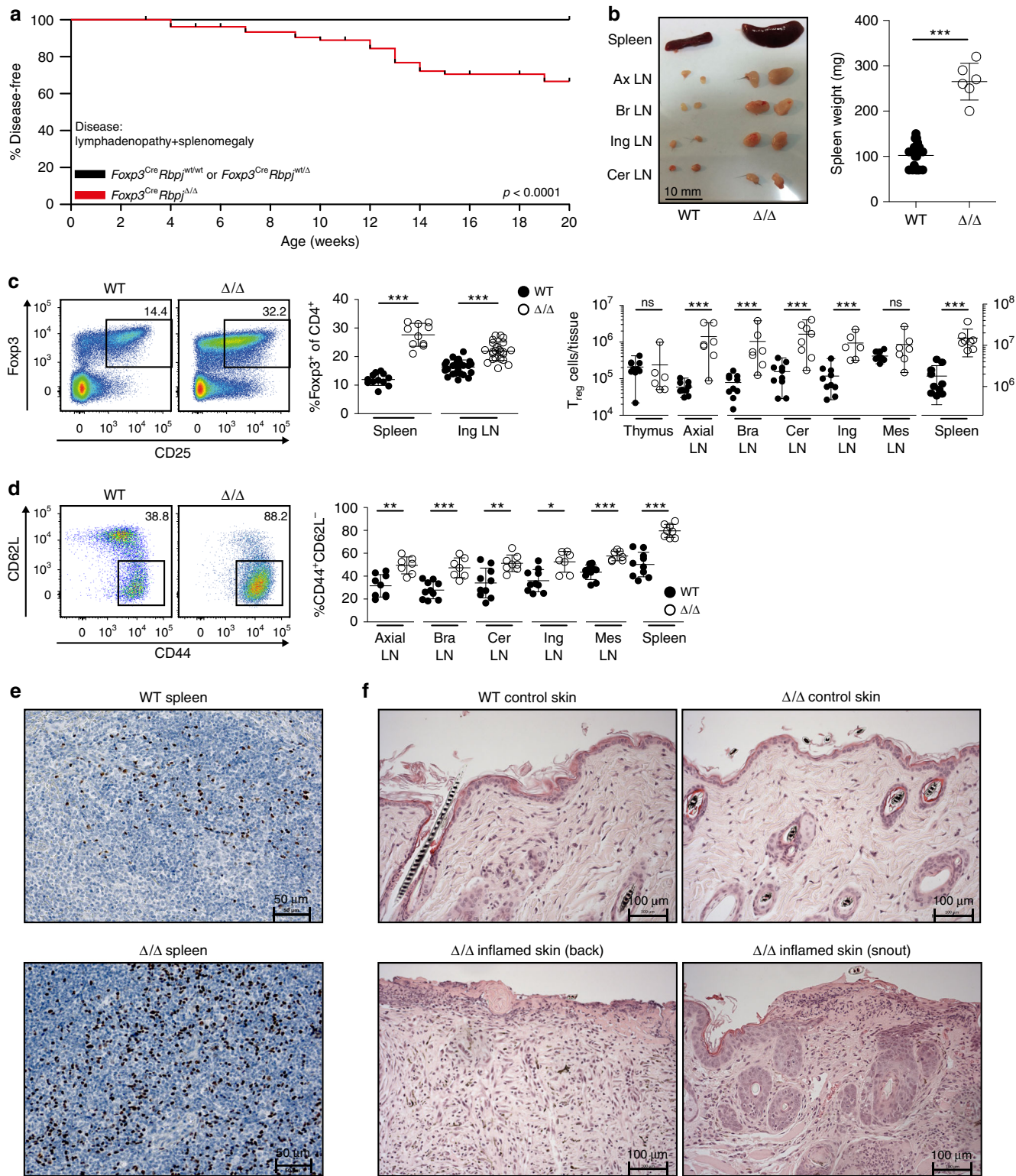
Deletion of *Rbpj* causes defined organ pathology. We specifically deleted *Rbpj* in T_{reg} cells by crossing *Foxp3^{Cre,YFP}* mice with mice harboring floxed *Rbpj* alleles (called Δ/Δ). We compared these to littermate control *Foxp3^{Cre,YFP}* mice with wildtype *Rbpj* alleles (termed WT). We closely monitored our mice for 20 weeks, and about 40% of mice spontaneously developed splenomegaly and lymphadenopathy within this time interval, while about 60% of animals remained healthy (Fig. 1a, b). We confirmed the T_{reg} -specific deletion of *Rbpj* on DNA, RNA, and protein level (Supplementary Fig. 1a–d). First, we analyzed Δ/Δ and WT mice for the presence of $CD4^+CD25^+Foxp3^+$ T_{reg} cells in spleen and other tissues (Fig. 1c). We observed a strong increase in the fraction of T_{reg} cells among $CD4^+$ T cells from about 12% in WT spleens to 28% in spleens from affected Δ/Δ animals. In absolute numbers, lymph nodes and spleen from Δ/Δ animals harbored about 10–20 times more T_{reg} cells than their WT counterparts (Fig. 1c, right panel). This increase was not seen in the thymus, indicating normal thymic T_{reg} cell output, or in mesenteric lymph nodes. Analysis of CD44 and L-selectin (CD62L) indicated activation of the T_{reg} compartment in

affected Δ/Δ mice (Fig. 1d). Furthermore, affected Δ/Δ animals showed a higher density of Foxp3-positive T_{reg} cells by immunohistology in spleen (Fig. 1e) and lymph nodes (Supplementary Fig. 1e). Affected animals developed noticeable skin pathology at snout, abdominal and tail regions, which served as useful biomarker to identify sick animals. Affected skin areas showed thickening of the epidermis and mononuclear cell infiltrates in the corium (Fig. 1f). Global defects in T_{reg} cell function normally lead to a severe autoimmune manifestation, with destructive immune cell infiltration in a diverse set of organs². Detailed histological examination of different organs including small intestine, large intestine, stomach, kidneys, salivary gland, eye, liver, and lung showed no signs of obvious immune cell infiltration and tissue destruction (Supplementary Figure 2a, b), indicating that *Rbpj* deficiency in T_{reg} cells did not lead to a global loss of T_{reg} -mediated immune control. This was supported by data from a standard in vitro suppression assay with TCR-stimulated $T_{responder}$ cells, where we did not detect significant changes in the in vitro suppressive potential (Supplementary Fig. 3). In summary, these data indicate that RBPJ deficiency affected a more specific segment of T_{reg} function.

Germinal center formation and B-cell polarization. Given that the T_{reg} -specific deletion of *Rbpj* affected secondary lymphoid organs and skin, we performed gene expression analysis of total LN RNA from WT and affected Δ/Δ animals (Fig. 2a). The most strongly up-regulated genes among the 4388 differentially expressed probes were involved in immune globulin (Ig) chain rearrangement and antibody production (Fig. 2a, highlighted in blue). Furthermore, B cell-specific markers such as *Cd22* and *Cd19* were over-expressed in LN from Δ/Δ mice. In addition, *Il4* was increased and pointed towards T_H2 subtype polarization (Fig. 2a and Supplementary Fig. 4a). B cells also down-modulated CD62L, and total numbers of B cells expanded about 10–20-fold in affected animals (Fig. 2b). To determine whether this increase in absolute B cell numbers and their maturation lead to changes in antibody Ig subtype distribution, we analyzed blood serum Ig levels via ELISA (Fig. 2c). Interestingly, we detected a significant up-regulation of IgG1 and IgE, while IgG3 was repressed in the serum (Fig. 2c), indicative of a classical IL-4 (= T_H2)-induced B cell antibody class switch²¹. As another hallmark of ongoing B cell differentiation and antibody production, we detected the formation of numerous germinal centers in LNs from affected Δ/Δ animals, but not in healthy WT animals (Fig. 2d and Supplementary Fig. 4b). Since IgE levels showed an almost 100-fold increase in affected Δ/Δ animals (Fig. 2c), and skin-resident mast cells express a high-affinity IgE receptor, we performed Giemsa staining of affected skin tissue. Indeed, we found an accumulation of mast cells rich in dark-stained granulae, presumably contributing to skin pathology in Δ/Δ animals (Fig. 2e and Supplementary Fig. 4c).

Because of the spontaneous germinal center formation, we analyzed whether the produced antibodies could bind self-antigens. To this end, protein was extracted from different organs isolated from *Rag2*-deficient animals, separated by SDS-PAGE, and incubated with serum from WT or affected Δ/Δ animals. We observed antibody binding to self-proteins extracted from organs such as lung, stomach, small intestine, pancreas, and eye with blood serum from Δ/Δ animals, although antibody-binding patterns were different between individual animals (Supplementary Fig. 5). In conclusion, our B-cell analysis revealed spontaneous germinal center formation with T_H2 -specific Ig class-switch.

T_H2 polarization of T_{conv} cells. *Il4* expression was increased in LN from Δ/Δ mice (Fig. 2a and Supplementary Fig. 4a), therefore



we studied T_{conv} polarization. In spleen and LN, T_{conv} cells became activated and differentiated into effector/memory T cells by down-regulation of CD62L and up-regulation of CD44. Furthermore, the absolute number increased by about 5–10-fold (Fig. 3a). Treatment of T cells from WT and affected Δ/Δ animals with phorbol-12-myristate-13-acetate (PMA) and Ionomycin to measure intracellular cytokine expression revealed higher frequencies of T_{conv} cells from affected Δ/Δ animals producing IL-2, IL-4, and IL-13, while T_{reg} cells remained unchanged (Fig. 3b).

This indicated a T_H2 polarization. Since Gata-3 is the master transcription factor of T_H2 cells, we analyzed Gata-3 expression in the T_{conv} compartment and detected increased frequencies of Gata-3-positive T_{conv} cells from about 3% in WT to 13% in Δ/Δ animals by flow cytometry (Fig. 3c, d), which was confirmed on RNA level (Fig. 3d, right panel). Co-staining of stimulated T_{conv} cells with IL-4, IL-13, and Gata-3 revealed that IL-4 and IL-13 was mainly produced by Gata-3-positive T_H2 cells (Fig. 3c). To examine closely the link between the observed T_H2 bias and the

Fig. 1 T_{reg} -specific deletion of *Rbpj* causes lymphoproliferative disease. **a** Kaplan–Meier survival curve illustrating disease development in *Foxp3^{Cre}Rbpj^{Δ/Δ}*, *Foxp3^{Cre}Rbpj^{wt/Δ}*, and *Foxp3^{Cre}Rbpj^{wt/wt}* animals within 20 weeks after birth. Disease defined by inflammatory skin lesions, lymphadenopathy, and splenomegaly. We observed 79 animals with T_{reg} lineage-specific bi-allelic *Rbpj* deletion (*Foxp3^{Cre}Rbpj^{Δ/Δ}*), 67 animals with mono-allelic *Rbpj* deletion (*Foxp3^{Cre}Rbpj^{wt/Δ}*), and 79 wildtype animals (*Foxp3^{Cre}Rbpj^{wt/wt}*). Statistical testing log-rank Mantel–Cox test ($p < 0.0001$). T_{reg} -specificity of *Rbpj* deletion in Supplementary Fig. 1. **b** Splenomegaly and lymphadenopathy in affected Δ/Δ animals, representative picture (Ax: axial; Br: brachial; Ing: inguinal; Cer: cervical). Right panel, spleen weight in milligram ($n = 6–19$, Mann–Whitney test) in a dot plot where error bars indicate standard deviation and center line mean value. **c** Quantification of T_{reg} ($CD3^+CD4^+CD8^-CD25^+Foxp3^+$) cell number and frequency in WT vs. affected Δ/Δ animals. Left panel, representative pseudocolor plots of splenic T_{reg} cells of $CD4^+$ T cells, frequencies shown as number. Middle graph, T_{reg} frequencies in spleen and LN (% of $CD4^+$, $n = 6–26$, Mann–Whitney test). Black dots T_{reg} cells from WT, open circle dots T_{reg} cells from Δ/Δ animals, dots represent individual mice, line mean value. Right graph, total T_{reg} cell numbers in various tissues ($n = 6–10$, Mann–Whitney test, Mes: mesenteric). **d** Left panel, CD44 and CD62L expression in T_{reg} cells from spleens of WT and affected Δ/Δ animals, quantification for several tissues to the right ($n = 7–10$, Mann–Whitney test). **e** Immunohistochemistry (IHC) of spleen from WT and affected Δ/Δ animals. Foxp3 staining in brown with hematoxylin staining. **f** Hematoxylin and eosin (H&E) staining of non-inflamed and inflamed skin tissue of representative WT and affected Δ/Δ mouse. Additional stainings in Supplementary Fig. 2. Data representative of two or more independent experiments with individual mice. Asterisks indicate statistical significance with $***p < 0.001$, $**p < 0.01$, and $*p < 0.05$. In IHC and H&E stainings, original magnification scale bars have been magnified for better visibility. Source data are provided as a Source Data file

profound B cell phenotype, we analyzed T-follicular helper (Tfh) cells in LNs by Cxcr-5 and PD-1 co-staining. We observed an increase in the Cxcr-5⁺PD-1⁺ Tfh cell fraction and total numbers (Fig. 3e). Furthermore, we identified significantly more Gata-3-polarized Tfh cells in Δ/Δ animals (Fig. 3f).

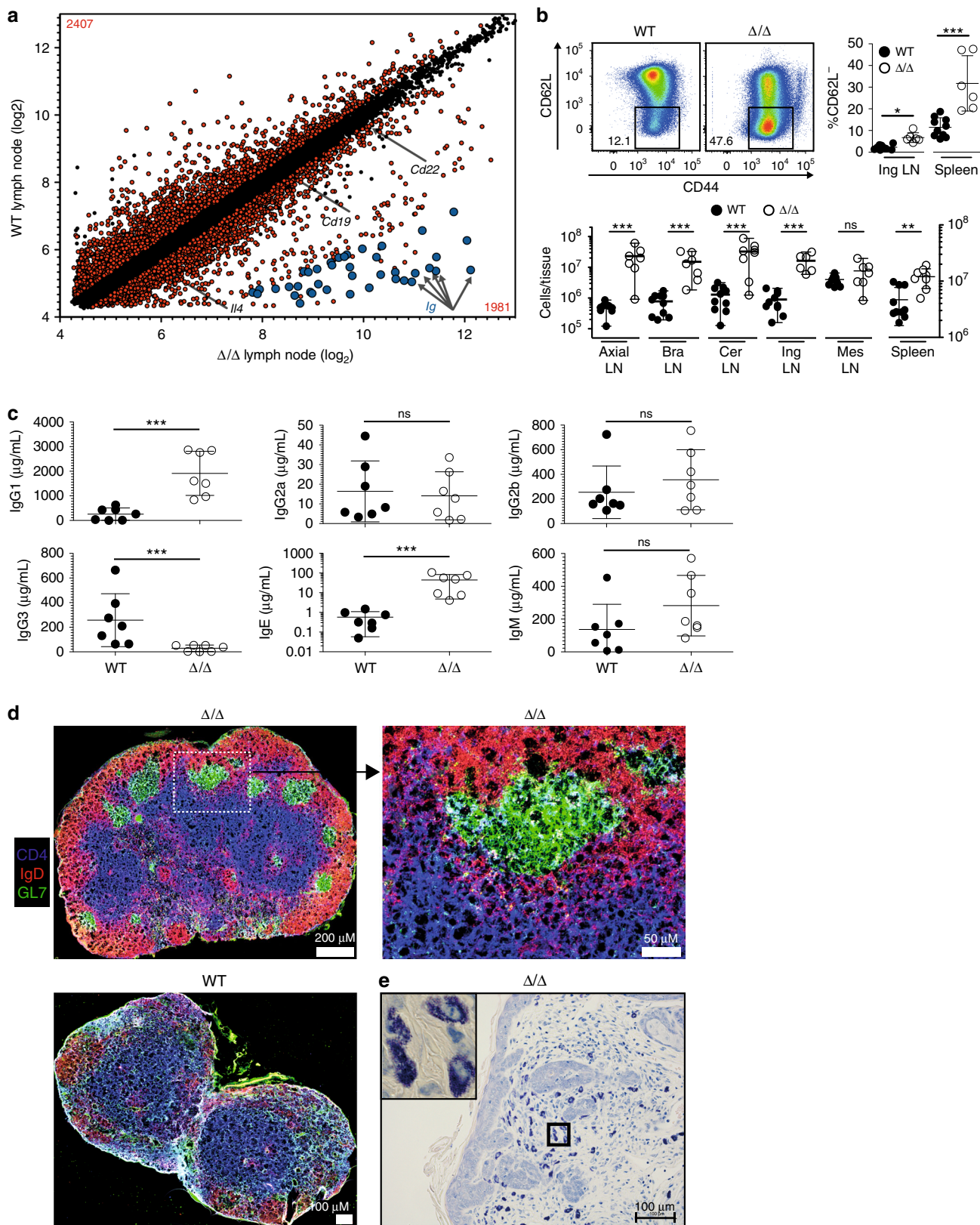
Environmental conditions influence disease development.

Approximately 40% of *Foxp3^{Cre},YFP**Rbpj^{Δ/Δ}* mice developed a T_{H2} -polarized disease, while 60% of animals did not get sick during a 20-week observation period (Fig. 1a). Since most mice that developed a pathology were older than 10 weeks, environment-related causes might influence the phenotype in Δ/Δ animals. Therefore, we transferred embryos into a new breeding facility with individually ventilated cages and a defined altered Schaedler flora (details in Methods section). In this new environment, the incidence rate dropped and about 90% of animals remained healthy until 20 weeks of age (Fig. 4a). These findings indicate that environmental factors influence T_{H2} -disease onset in Δ/Δ animals. To further investigate this, we infected healthy young Δ/Δ and control animals from the new breeding facility with the parasitic nematode *Strongyloides ratti* (*S. ratti*). Infective larvae penetrate the skin and migrate within 3 days to the small intestine. Normally, immune competent mice mount a canonical T_{H2} response and resolve the infection within 2–4 weeks²². Final expulsion of parasites from the intestine is predominantly mediated by IL-9 and activated mucosal mast cells²³. Especially, Foxp3⁺ T_{reg} cells have been shown to expand following *S. ratti* infection²⁴. Therefore, we infected two cohorts of Δ/Δ and WT animals with *S. ratti* infectious larvae into the footpad and examined animals after 6 (cohort 1) and 14 days (cohort 2, Fig. 4b). Already 6 days post infection (p.i.), T_{reg} frequency of $CD4^+$ T cells in the spleen increased in Δ/Δ animals to about 28%, while WT animals had normal T_{reg} frequencies at that time point (about 9%) (Fig. 4c). The three-fold increase in T_{reg} frequency was persistent and also measured at 14 days p.i. (Fig. 4c). At the 14-day time point, T_{conv} cells expressed more Gata-3 in Δ/Δ animals (Fig. 4d), as well as more IL-4, IL-13, and IL-9, but not IFN- γ (Fig. 4e–g). The fraction of Gata-3-high expressing T_{reg} cells increased in the Δ/Δ animals from day 6 to day 14 p.i. to 56%, while at the same 14-day time point, the WT animals had significant lower numbers (27%, Fig. 4d). Furthermore, we detected increased levels of IgE, but not IgM, in blood serum of Δ/Δ animals (Fig. 4h), mirroring the phenotype observed during our initial breeding (Fig. 2c). Interestingly, on day 6, Δ/Δ animals with stronger T_{H2} -polarization and increased IL-9 production displayed reciprocally reduced output of *S. ratti* DNA (Fig. 4i) and a strong trend towards reduced numbers of

parasitic females in the intestine (Fig. 4j). In summary, our data indicate that disease development in Δ/Δ animals was influenced by environmental factors, such as the breeding environment, and that the T_{H2} -inducing parasite *S. ratti* could trigger the onset of this phenotype in Δ/Δ animals.

Characterization of *Rbpj*-deficient T_{reg} cells. Mice with *Rbpj*-deficiency in T_{reg} cells spontaneously developed a T_{H2} -type disease. Since the *Rbpj*-deficiency was specific to T_{reg} cells, we aimed at dissecting the molecular properties of those. Therefore, we measured the expression of classical T_{reg} associated proteins, such as Foxp3, cytotoxic T-lymphocyte-associated protein 4 (Ctla-4), or Ikaros family zinc finger 2 (Helios), and did not detect obvious differences between T_{reg} cells from WT or affected Δ/Δ animals (Fig. 5a). Analogously, the methylation status of the T_{reg} -specific demethylated region (TSDR), a well-described methylation-sensitive *cis*-regulatory region required for durable expression of the *Foxp3* gene²⁵, was unchanged (Fig. 5b). The investigation of the T cell receptor (TCR) repertoire revealed no abnormal TCR beta J-chain usage (Fig. 5c), nor any dominant clones (Fig. 5d), and only a small increase in overall clonality and decreased entropy (Fig. 5e). As T_{reg} cells were abundantly present in lymphatic organs of affected Δ/Δ animals, we analyzed peripheral tissues. T_{reg} frequency and total numbers were either equal or elevated (40-fold in affected skin tissue and about three-fold in the lung, Fig. 5f–g and Supplementary Fig. 6) in affected Δ/Δ animals. Since T_{reg} cells co-opt parts of T_H subset programs to specifically suppress those T_H subset responses, we analyzed Gata-3 protein expression. Indeed, we could detect a strong increase of Gata-3 high-expressing T_{reg} cells isolated from affected Δ/Δ compared to WT animals (about 45% vs. 12%, respectively), which could be confirmed on RNA level (Fig. 5h). Furthermore, we investigated T follicular regulatory cells based on the expression of Cxcr5⁺ and PD1⁺ (Tfr; $CD4^+CD25^+Foxp3^+Cxcr5^+PD1^+$) in WT and Δ/Δ animals. The total number of PD1⁺ Tfr cells was increased in LNs of affected Δ/Δ animals (Fig. 5i), excluding the possibility that a loss of Tfr cells was responsible for the observed phenotype. In addition, we co-stained PD-1 and Gata-3 and noticed a strong increase in Gata-3⁺PD-1⁺ T_{reg} cells in Δ/Δ mice (Fig. 5j).

Altered gene expression in *Rbpj*-deficient T_{reg} cells. To dissect molecular characteristics, we performed array-based gene expression analysis of T_{reg} cells isolated from affected Δ/Δ and WT animals (Fig. 6a). Six hundred and ninety probes were found to be differentially expressed. For example, we observed a strong up-regulation of IL-7 receptor (*Il7r*) and Killer cell lectin-like receptor subfamily G member 1 (*Klrg1*) genes, while Bcl-2-like



protein 11 (*Bcl2l1*) and Deltex-1 (*Dtx1*) were under-represented in Δ/Δ T_{reg} cells (Fig. 6a, b). *Bcl2l1* serves as translocator of apoptosis-inducing factors and regulator of mitochondrial depolarization^{26,27}. Indeed, Rbpj-deficient T_{reg} cells showed less caspase-3 activity when compared to WT T_{reg} cells (Fig. 6c and Supplementary Fig. 7). Besides differences in apoptosis, Rbpj-

deficient T_{reg} cells also up-regulated the *Il7r* gene encoding for the IL-7 receptor (IL-7R, CD127). In thymus and spleen, about 75% of T_{conv} cells expressed the IL-7R, and this was not different in WT and Δ/Δ animals. In contrast to this, T_{reg} cells from Δ/Δ mice showed a strong increase in IL-7R expression in the spleen (Fig. 6d). Since the IL-7R is involved in survival and

Fig. 2 Analysis of B cell involvement. **a** Gene expression profile of LNs from WT vs. affected Δ/Δ animals. Significantly different probes colored in red and numerated in corners ($p < 0.05$), three biological replicates per group. Of 50 most up-regulated probes in Δ/Δ LNs, 38 probes annotated Ig-related genes (highlighted blue). Statistical testing described in Methods section. For few genes, differential expression confirmed in Supplementary Fig. 4. **b** Upper left panel, representative dot plots of CD62L and CD44 expression of splenic B cells ($CD3^+CD4^-CD8^-CD19^+$) from WT vs. affected Δ/Δ animals, quantification for spleen and LN B cells to the right ($n = 6-10$, Mann-Whitney test). Lower panel absolute B cell numbers per lymph node or total spleen ($n = 6-10$, Mann-Whitney test). Black dots B cells in WT animals, open circles Δ/Δ -mice, individual mice are shown. **c** Ig subtype analysis of antibodies in peripheral blood serum of WT vs. affected Δ/Δ animals. Ig subtype levels detected by ELISA. Statistical testing with Mann-Whitney test ($n = 7$). **d** Immunohistochemistry of lymph nodes from WT and affected Δ/Δ animals. CD4 staining in blue, IgD staining in red, and GL7 staining in green. Top left image scanned lymph node from Δ/Δ animal. Typical germinal center highlighted with box and enlarged in image to the right. At bottom left, image of WT lymph node. All images recorded with same settings and color intensity adjustments. Additional wildtype stainings in Supplementary Fig. 4. **e** Giemsa staining of skin tissue from affected Δ/Δ animal. Granule-rich mast cells stained in blue. Mast cell enriched area outlined by rectangle, enlarged on the upper left quadrant of image. Additional wildtype stainings in Supplementary Fig. 4. Data are representative of two or more independent experiments with individual mice (**b**) or a single experiment with individual mice (**a, c, d, e**). In IHC and Giemsa stainings, original magnification scale bars magnified for better visibility. Source data are provided as a Source Data file

proliferation²⁸, we correlated IL-7R expression with the overall frequency of T_{reg} cells in unaffected, as well as phenotypically affected Δ/Δ animals of varying age. A good correlation between both parameters could be observed ($r = 0.81$), suggesting that IL-7R expression supports T_{reg} accumulation (Fig. 6e). To further validate this, we co-stained IL-7R expression with KI-67, a widely accepted cell proliferation marker²⁹ (Fig. 6f). The majority of T_{reg} cells in Δ/Δ animals expressed both IL-7R and KI-67, which was not seen in WT animals (Fig. 6f), indicating that IL-7R high-expressing T_{reg} cells were the proliferating fraction in Δ/Δ animals. Next, we measured the phosphorylation of Stat-5, a downstream component of the IL-7R signaling cascade³⁰. With escalating doses of IL-7, Rbpj-deficient T_{reg} cells phosphorylated significantly more Stat-5, indicating elevated cytokine sensitivity (Fig. 6g). Since *Klrg1* was up-regulated in the gene expression profile (Fig. 6a), we co-stained *Klrg1* and IL-7R expression (Fig. 6h). Indeed, while a *Klrg1*⁺IL7R⁺ double-positive population was almost absent in T_{conv} cells or WT T_{reg} cells, the spleens of affected Δ/Δ animals harbored about 60% *Klrg1*⁺IL7R⁺ T_{reg} cells (Fig. 6h). Therefore, both IL-7R and *Klrg1* were valuable parameters to identify the intensively proliferating subpopulation of T_{reg} cells in affected Δ/Δ mice.

IL-7R⁺*Klrg1*⁺ T_{reg} cells are reminiscent of *tisT_{reg}ST2*. In a recent publication, we described a tissue-resident T_{reg} population characterized by the expression of, amongst others, IL-7R, *Klrg1*, IL-33 receptor alpha (ST2), and *Gata-3*⁷. This T_{reg} subset, mainly present within tissues and T_H2 -polarized, was called *tisT_{reg}ST2*⁷. Since we detected a strong enrichment of *Gata-3*, *Klrg1*, and IL-7R-expressing T_{reg} cells specifically in affected Δ/Δ animals, we performed a co-staining for ST2 and *Klrg1* (Fig. 7a). About 2% of T_{reg} cells from spleens of WT animals co-express ST2 and *Klrg1* compared to 50–60% of spleen T_{reg} cells from affected Δ/Δ animals (Fig. 7a). A co-staining with KI-67 and *Gata-3* revealed that *Klrg1*⁺ST2⁺ T_{reg} cells in both WT and Δ/Δ animals were T_H2 polarized and proliferating (Fig. 7a, middle panel). *Klrg1*⁺ST2⁺ were also significantly increased in lymph nodes (WT: 2%, Δ/Δ : 27%) and skin tissue (WT: 48%, Δ/Δ : 65%, Fig. 7b). To compare the tissue-like gene expression program of *Klrg1*⁺ *tisT_{reg}ST2*-like cells in Δ/Δ animals on a broader scale, we sorted Δ/Δ *Klrg1*⁺, Δ/Δ *Klrg1*⁻, WT *Klrg1*⁺ and WT *Klrg1*⁻ T_{reg} cells from spleen and performed RNA sequencing (RNA-seq) analysis. We extracted RNA-seq data from fat, skin and LN-derived bulk T_{reg} cells from a previous study⁷ and normalized all datasets. We then plotted 106 reported *tisT_{reg}ST2* genes in a heatmap (Fig. 7c). Interestingly, there was a strong gene expression overlap between fat and skin T_{reg} -differentially regulated genes with spleen Δ/Δ -derived and WT-derived *Klrg1*⁺ T_{reg} cells, indicating that the majority of Δ/Δ - T_{reg} cells from affected mice indeed displayed a

tisT_{reg}ST2-like signature. Still, when listing key genes identifying tissue T_{reg} cells from fat (*Pparg*) or skin (*Gpr55*), as well as tissue T_{reg} effector molecules such as *Il10* and amphiregulin (*Areg*), the Δ/Δ *Klrg1*⁺ *tisT_{reg}ST2*-like population in the spleen of Δ/Δ animals did not express comparable levels of these markers (Fig. 7d). This indicated that they were generated in the lymphoid tissue rather than extravasated from non-lymphoid tissues. To analyze differences in more detail, we prepared MA plots for comparisons between all four groups (Fig. 7e). The comparison between WT *Klrg1*⁺ vs. Δ/Δ *Klrg1*⁺ T_{reg} cells revealed 2036 differential expressed genes, which include the molecular changes associated with loss of *Rbpj* (Fig. 7e; left panel). This group contains well-known *Rbpj* target, such as *Dtx1*^{31,32}, as well as suppression-related proteins such as *Id-3*³³. The comparison between WT *Klrg1*⁻ vs. Δ/Δ *Klrg1*⁺ T_{reg} cells revealed 3330 differential expressed genes (Fig. 7e; right panel), which include tissue- T_{reg} -related genes, such as *Klrg1* and *Il1rl1*, as well as suppression-related proteins such as *Bach2*³⁴. In summary, we showed that affected Δ/Δ animals harbor a strongly increased *tisT_{reg}ST2*-like population in their lymphoid tissues.

Genome-wide chromatin accessibility of WT and Δ/Δ T_{reg} cells.

In affected Δ/Δ animals, *Klrg1*⁺ tissue-like T_{reg} cells constitute the majority of all spleen T_{reg} cells, while in WT animals, *Klrg1*⁻ non-tissue T_{reg} cells dominate the T_{reg} pool at large. To obtain insights into their gene-regulatory landscapes, we isolated both populations and performed the Assay for Transposase-Accessible Chromatin using sequencing (ATAC-seq)³⁵. In total, across cell types and replicate experiments, we detected 68,214 ATAC-seq peaks throughout the genome (Fig. 8a). Reference genome annotation revealed that 17.5% of the peaks located to promoters, 41.5% to introns, 2.0% to exons, and 39% to intergenic genomic regions (Fig. 8b). In Δ/Δ T_{reg} cells, about 3400 regions were more accessible compared to WT T_{reg} cells, while in WT T_{reg} cells, 10,816 regions were more accessible in comparison to Δ/Δ T_{reg} cells (Fig. 8b, c). We next asked which transcription factor motifs were enriched in differential accessible chromatin regions to identify potential drivers of WT-specific and Δ/Δ T_{reg} -specific gene-regulatory programs. De novo motif analysis revealed a strong *Gata* transcription factor signature in Δ/Δ T_{reg} -specific regions (24.38%) vs. background sequences (13.22%) with a high *p*-value (10^{-68}) and score (0.95) (Fig. 8d, Supplementary Fig. 8a). Of the relevant *Gata* family members, only *Gata-3* was significantly induced in Δ/Δ T_{reg} cells (Fig. 8d, lower panel). In addition, we identified enrichment of *Ets*, *Klf*, and *AP-1*-binding sites in Δ/Δ T_{reg} -specific regions (Supplementary Fig. 8a). WT T_{reg} -specific regions were dominated by *Ets*, *Tcf*, *Stat*, as well as *Nur77* motifs, and we also identified significant enrichment of a motif highly similar to the recently described *Rbpj* consensus-

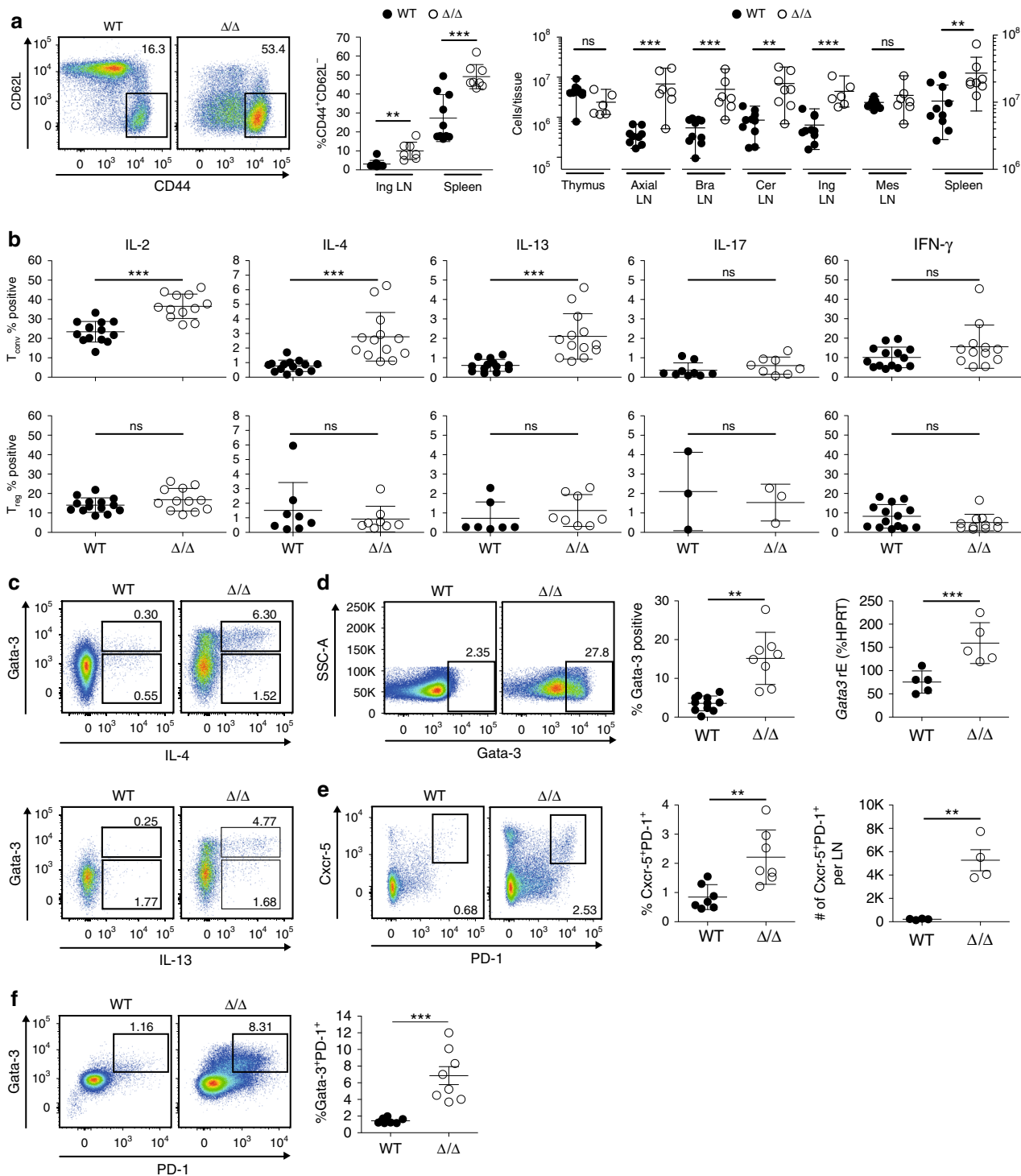
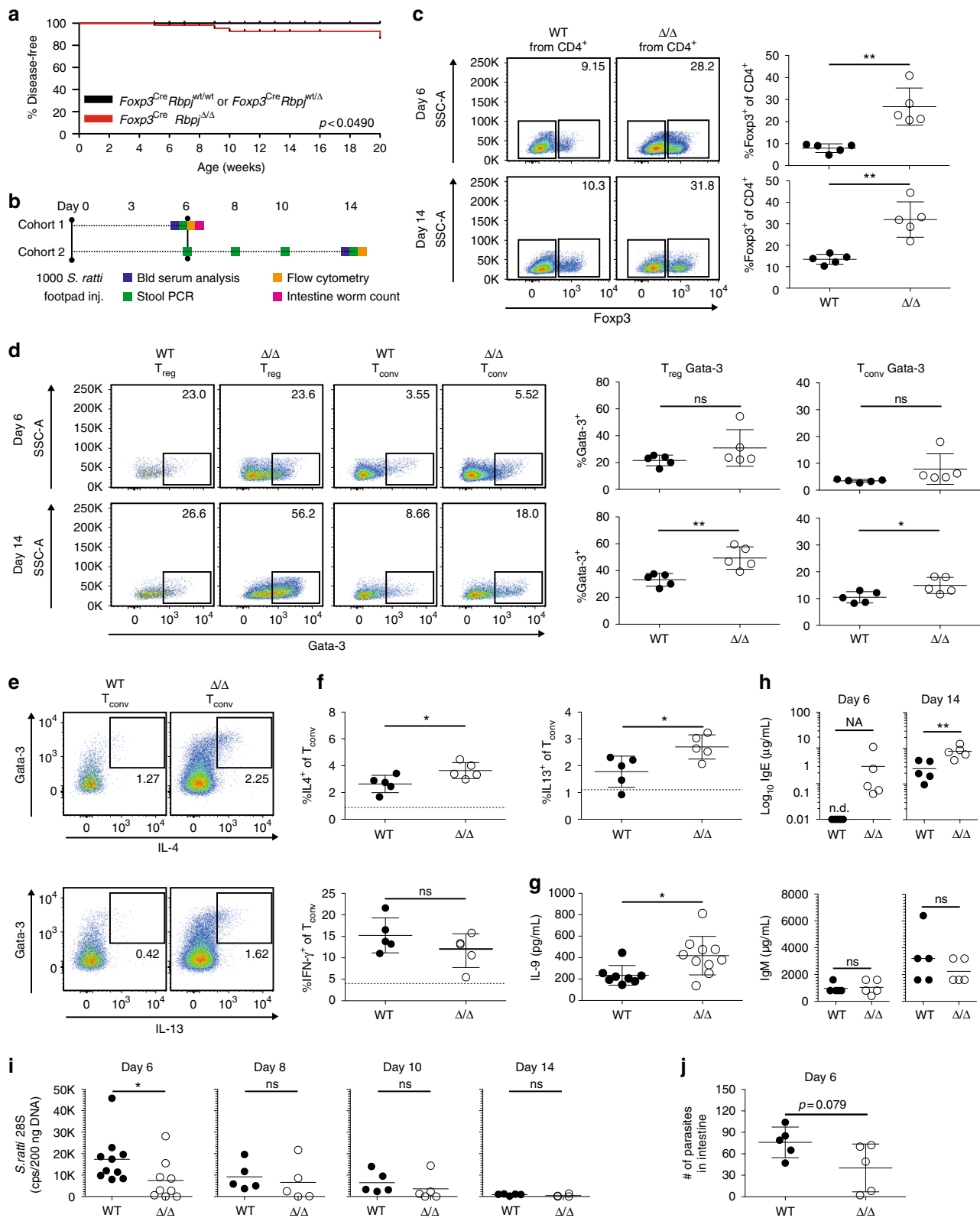


Fig. 3 T_{conv} cells derived from affected Δ/Δ animals are T_{H2} polarized. **a** T_{conv} cells (CD3⁺CD4⁺CD25⁻Foxp3⁻) from spleens of WT and affected Δ/Δ animals stained for CD44 and CD62L expression, quantification for spleen and LN ($n = 7-10$, Mann-Whitney test) adjacent to pseudocolor plots. Right panel, T_{conv} cell numbers per tissue ($n = 6-10$, Mann-Whitney test). Black dots T_{conv} cells in WT animals, open circles Δ/Δ -derived T_{conv} cells, individual mice are shown. **b** Restimulation of splenic T cells followed by intracellular cytokine staining. Upper panel intracellular cytokines in T_{conv} cells, lower panel in T_{reg} cells (CD3⁺CD4⁺CD25⁺Foxp3⁺). Statistical testing with Mann-Whitney test (IL-2: $n = 12-14$; IL-4: $n = 8-14$; IL-13: $n = 7-13$; IL-17: $n = 3-9$; IFN- γ : $n = 12-14$). **c** Co-staining of stimulated T_{conv} cells with cytokine and Gata-3 antibody. Upper panel representative dot plots of PMA/Ionomycin-stimulated WT (left) or Δ/Δ (right) T_{conv} cells, with IL-4 staining on X-axis and Gata-3 staining on Y-axis. Lower panel, IL-13 staining. **d** Left, dot plots of Gata-3 protein staining in spleen-derived T_{conv} cells; middle panel, quantification of Gata-3-positive cells (% of T_{conv}, $n = 8-11$, unpaired t -test); right panel, Gata3 mRNA in T_{conv} cells (% Hprt, $n = 5$, unpaired t -test). **e** Identification of T follicular helper cells in lymph nodes from WT vs. affected Δ/Δ animals. Tfh cells identified as CD3⁺CD4⁺CD8⁻CD25⁻Foxp3⁻Cxcr-5⁺PD-1⁺ T cells and quantified ($n = 7$, unpaired t -test). Total numbers of Tfh cells per LN to the right ($n = 4$, unpaired t -test). **f** CD3⁺CD4⁺CD8⁻CD25⁻Foxp3⁻ T cells in lymph nodes of WT or affected Δ/Δ animals co-stained with PD-1 and Gata-3. Quantification to the right ($n = 8$, unpaired t -test). Data are representative of two or more independent experiments with individual mice (**a**, **b**, **d**, **e**, **f**) or a single experiment with individual mice (**c**). Source data are provided as a Source Data file



binding site (Supplementary Fig. 8b). Examples of ATAC-seq signals along with occurrences of *Rbpj* motifs (both de novo identified and previously identified consensus motifs) at key genes are shown in Fig. 8e–h and Supplementary Fig. 8c. Earlier, we showed that *Foxp3* expression was unchanged between Δ/Δ and WT T_{reg} cells (Fig. 5a) and *Foxp3* TSDR demethylation was unaffected by loss of *Rbpj* (Fig. 5b). Accordingly, the ATAC-seq

profile at the *Foxp3* locus remained unchanged between both groups (Fig. 8e). Peak calling identified the TSDR region as highly accessible region in both WT and Δ/Δ T_{reg} cells, but no *Rbpj*-binding motif has been detected in this or any other part of the *Foxp3* gene. The *Rbpj* locus was accessible in both WT and Δ/Δ T_{reg} cells, indicating that *Rbpj* was not required to open its own locus (Supplementary Fig. 8c). In contrast to this, tissue- T_{reg} -

Fig. 4 Disease development in Δ/Δ animals is environment-related. **a** Kaplan–Meier curve illustrating disease development in WT vs. Δ/Δ animals within 20 weeks after birth as in Fig. 1a, but in different breeding environment (55 animals *Foxp3^{Cre}Rbpj Δ/Δ* , 45 animals *Foxp3^{Cre}Rbpj^{wt/wt}*, 40 animals *Foxp3^{Cre}Rbpj^{wt/wt}*). Statistical testing log-rank Mantel–Cox test ($p = 0.049$). **b** Parasitic infection regimen with *S. ratti*. Two cohorts, each 5 WT vs. 5 healthy young Δ/Δ animals, infected on day 0. End point for cohort 1, 6 days and cohort 2, 14 days post infection (p.i.). Experiments and parameter measurement intervals indicated. **c** Representative pseudocolor plots displaying *Foxp3* expression in WT vs. Δ/Δ spleen CD4⁺ T cells 6 or 14 days p.i.. Right, quantification of T_{reg} (CD3⁺CD4⁺Foxp3⁺) cell percentage of CD4⁺. Black dots WT, open circle Δ/Δ animals ($n = 5$, unpaired *t*-test). **d** Gata-3 staining in T_{reg} and T_{conv} (CD3⁺CD4⁺Foxp3⁻) cells from WT vs. Δ/Δ animals infected with *S. ratti* 6 or 14 days p.i., quantification right (%Gata-3⁺ of T_{reg} or T_{conv}, $n = 5$, unpaired *t*-test). **e** Co-staining of stimulated T_{conv} cells isolated from WT or Δ/Δ animals 14 days p.i. with IL-4 and IL-13 and Gata-3 antibody. **f** Quantification of intracellular cytokine expression in re-stimulated splenic T_{conv} cells ($n = 5$, unpaired *t*-test). Frequencies of IL-4, IL-13, and IFN- γ . Dotted line unstimulated, but transport inhibitor-treated levels. **g** Mesenteric LN cells of WT vs. Δ/Δ animals 6 and 14 days p.i. stimulated with anti-CD3 and detection of secreted IL-9 by ELISA ($n = 10$, unpaired *t*-test). **h** Ig subtype analysis of antibodies in peripheral blood serum of WT vs. Δ/Δ animals 6 or 14 days p.i. Ig subtype levels detected by ELISA ($n = 5$, paired *t*-test). **i** Copy numbers of *S. ratti* 28S DNA in 200 ng of mouse stool samples. Day 6, stool samples from both cohorts 1 and 2 ($n = 10$), on day 8, 10, and 14 only from cohort 2 ($n = 5$, unpaired *t*-test). **j** Total count of parasites in the intestine on day 6 (cohort 1, unpaired *t*-test). Data are representative of two independent experiments (cohorts) with several individual mice ($n = 5$). Source data are provided as a Source Data file

related genes, such as *Klrg1* or *Il1rl1* (ST2) showed significant ATAC-seq signals around the promoter and potential enhancer sites in Δ/Δ T_{reg} cells, and Rbpj-binding motifs were also found in these regions (Fig. 8f). These changes in ATAC-seq signals translated into enhanced expression of *Il1rl1* and *Klrg1* (Fig. 8i). In addition to tissue T_{reg}-related genes, T_{reg} suppressive function-associated genes, such as *Il2ra*, *Dtx1*, and *Bach2* also displayed a distinct ATAC-seq profile: in intragenic and/or enhancer sites, WT T_{reg} cells had enriched signals compared to Rbpj-deficient T_{reg} cells (Fig. 8g). Again, Rbpj-binding motifs were detected in differential peaks and ATAC-seq profiles correlated well with changes in gene expression: *Il2ra* gene expression was significantly down-modulated in Δ/Δ T_{reg} cells, and expression of *Dtx1* and *Bach2* was almost completely lost (Fig. 8i). Interestingly, *Bach2* has recently been described as a key transcription factor involved in regulating T_{H2} polarization by inhibiting Gata-3 expression³⁴. Other T_{H2}-polarized-related regions were also differentially accessible in Δ/Δ T_{reg} cells, e.g., the T_{H2} locus control region (*Rad50*), *Il10* and *Areg*, but the corresponding genes were not expressed (Fig. 8h, Fig. 7d and Supplementary Fig. 8c). Taken together, our data suggest that both Rbpj and Gata3 influence the expression of key tisT_{reg}ST2-related genes, and that the genomic deletion of Rbpj in concert with a Gata-3-inducing T_{H2}-type inflammatory environment lead to the massive differentiation and expansion of tisT_{reg}ST2-like cells in Δ/Δ animals.

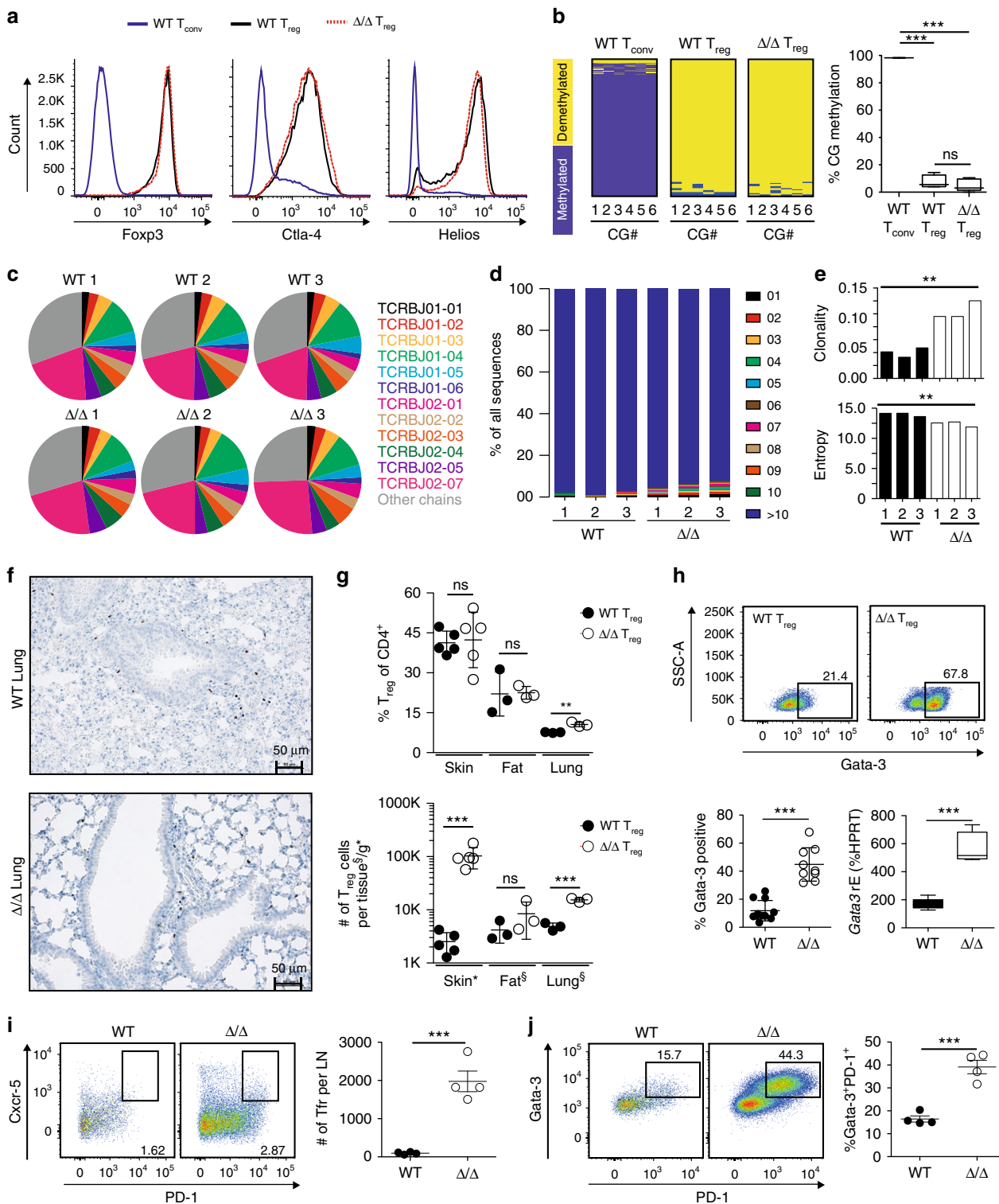
T_{H2}-polarized T_{reg} fail to suppress T_{H2} responses in vitro. But why are these T_{H2}-polarized T_{reg} cells not controlling the T_{H2}-response anymore? Recently, it was shown that *Lilrb4a* (encoding the protein ILT3) expressing T_{reg} cells were unable to regulate T_{H2}-responses due to their inability to control the maturation of a specific T_{H2}-promoting DC subset³⁶. This subset of DCs is characterized by the expression of PD-L2 and IRF-4^{36–38}. Our ATAC-seq data identified a highly accessible region at the *Lilrb4a* promoter in Klrg1⁺ST2⁺ T_{reg} cells isolated from affected Δ/Δ animals, and a Rbpj-binding site was also predicted in this region (Fig. 9a). Indeed, enhanced activity at the *Lilrb4a* promoter resulted in increased *Lilrb4a* expression in Klrg1⁺ST2⁺ T_{reg} cells from affected Δ/Δ animals (Fig. 9b). In addition, Klrg1⁺ST2⁺ T_{reg} cells from WT animals expressed more ILT-3 than Klrg1⁻ST2⁻ non-tissue type T_{reg} cells, suggesting a general mechanism of ILT3-expression during differentiation of the tisT_{reg}ST2-like gene expression program. Our de novo motif analysis indicated that Gata-3 was responsible for large parts of the tisT_{reg}ST2-like signature in Klrg1⁺ST2⁺ T_{reg} cells from affected Δ/Δ animals (Fig. 8d). To study the link between ILT3⁺Gata-3 overexpression and control of T_{H2} responses, we performed in vitro polarization studies with T_{reg} cells. IL-4 is the prototype cytokine to induce

Gata-3 expression and T_{H2} differentiation, and IL-33 is linked to the generation of tisT_{reg}ST2 cells⁷. Therefore, we FACS-sorted highly pure T_{reg} cells from *Foxp3^{GFP}* animals and expanded them with anti-CD3/CD28 microbeads, IL-2, IL-4, and IL-33 or without the latter two cytokines as control, for 6 days. Both groups of expanded T_{reg} cells stayed highly Foxp3 positive (Fig. 9c). Interestingly, we were able to co-induce ILT3 and Gata-3 expression specifically in the IL-4 and IL-33-treated T_{reg} cells (Fig. 9c). Using this model, we studied the ability of ILT3-expressing T_{H2}-polarized T_{reg} cells to influence DC maturation and DC-mediated T_{H2} polarization of FACS-sorted CD4⁺Foxp3⁻CD62L⁺ naive T cells in vitro. Our data revealed that ILT3-expressing T_{H2}-polarized T_{reg} cells profoundly promoted the differentiation of PD-L2⁺IRF4⁺ DCs, a subset described to support T_{H2} polarization in vivo^{36–38} (Fig. 9d). In addition, ILT3-expressing T_{reg} cells were unable to suppress the T_{H2} differentiation of IL-4 and anti-CD3-stimulated naive T cells into Gata-3-polarized effector T cells in the presence of DCs (Fig. 9e). These data strongly indicate that overexpression of Gata-3 and ILT3 renders T_{reg} cells less able to suppress T_{H2} responses in vitro. Finally, we investigated the sensitivity of Rbpj-deficient T_{reg} cells to T_{H2}-inducing conditions. To this end, we FACS-sorted and expanded Rbpj-deficient T_{reg} cells from healthy, young animals, with no pre-existing T_{H2} polarization, and compared them to WT T_{reg} cells. Both groups were treated with escalating doses of IL-4 in vitro (Fig. 9f). Indeed, Rbpj-deficient T_{reg} cells were more sensitive to the T_{H2}-inducing IL-4 treatment, translating into enhanced Gata-3 protein and mRNA induction in Δ/Δ T_{reg} cells (Fig. 9f). This elevated sensitivity towards Gata-3 induction could explain the profound expansion of Gata-3⁺Klrg1⁺ST2⁺ T_{H2}-polarized T_{reg} cells in affected Δ/Δ animals, with ameliorated T_{H2}-suppressive potential.

Discussion

In this study, we identify a previously unrecognized role for Rbpj in T_{reg} cell-mediated immune homeostasis. Upon T_{reg}-specific Rbpj deletion in *Foxp3^{Cre}Rbpj Δ/Δ* animals, mice developed a lymphoproliferative disease with type-2 effector polarized B-cell and T-cell responses. Disease development was environment-related and could be induced by infection with the parasitic nematode *S. ratti*. The finding that disease development was environment-related could explain the discrepancy to a published study using mice with *Rbpj Δ/Δ* T_{reg} cells, where the authors did not report the lymphoproliferative characteristic²⁰.

But what happened once the proper environmental trigger has been received? Based on our data, we would argue that deleting Rbpj confined the functional capacity of T_{reg} cells in several ways. First, augmented proliferation potential: the down-modulation of



Bcl2l11 could lead to enhanced resistance to apoptosis^{26,27}, while the up-regulation of the Interleukin-7 receptor promoted proliferation and supported a strong increase in total T_{reg} numbers in lymphoid tissues. Potential Rbpj-binding sites at the *Il7r* promoter region have already been reported³⁹. Second, Rbpj is important to restrict the T_H2 differentiation potential of T_{reg} cells: Rbpj-deficient T_{reg} cells were more sensitive to IL-4 polarization and concomitantly overexpressed Gata-3 and other T_H2 -associated proteins compared to WT T_{reg} cells. This was also observed upon in vivo infection with parasitic nematodes. Our

data showed that about two-times more T_{reg} cells expressed high levels of Gata-3 in $\Delta\Delta$ mice as compared to infected WT mice. As a consequence of Gata-3 expression, $\Delta\Delta T_{reg}$ cells differentiated into T_H2 -polarized Klrp1 $^+$ ST2 $^+$ $tisT_{reg}$ ST2-like cells. This differentiation integrated a third critical restriction of T_{reg} function and suppressive capacity: the loss of T_H2 -suppressive capacity via the down-modulation of *Bach2*, *Dtx1*, and *Il2ra*, and the induction of *IlT3*. *Il2ra*, encoding for the IL-2 receptor alpha chain (CD25), is required for T_{reg} suppressive capacity⁴⁰. *Bach2* has been described as an important transcription factor required

Fig. 5 Characterization of T_{reg} isolated from WT vs. affected Δ/Δ animals. **a** Representative histograms of Foxp3, Ctla-4, and Helios expression in Δ/Δ T_{reg} from affected animal (red dotted line), WT T_{reg} (black line), and WT T_{conv} (blue line). **b** Methylation of T_{reg} -specific demethylated region in T_{reg} and T_{conv} cells from WT and affected Δ/Δ animals. Yellow color indicates demethylated, blue methylated CpG dinucleotides. Total sequencing reads 2211 for WT T_{conv} , 67 for WT T_{reg} , and 129 for Δ/Δ T_{reg} . Statistical analysis one-way ANOVA and Bonferroni post-test ($n = 2-6$) in boxplots with center line (median), box (25-75 percentile) and standard deviation (min to max). **c** Pie charts illustrating TCR beta J-chain usage of T_{reg} cells from WT vs. affected Δ/Δ animals. Colors indicate respective TCR beta J-chain. Individual mice are shown ($n = 3$). **d** Frequency of 10 most abundant T_{reg} TCR sequences for each individual mouse from WT and affected Δ/Δ animals. All remaining sequences in blue. **e** Clonality (left) and entropy (right) values for all TCR sequences. Statistical testing unpaired t -test, individual mice are shown ($n = 3$). **f** Foxp3 staining in lung tissue sections from WT (left) or affected Δ/Δ animals (right). Additional Foxp3 stainings and controls in Supplementary Fig. 6. **g** Measurement of T_{reg} cell in peripheral tissues. T_{reg} (CD3⁺CD4⁺CD8⁻TCRb⁺CD25⁺Foxp3-GFP⁺) percentage of CD4⁺ (left) or total number (right) in respective tissue ($n = 5$, unpaired t -test). **h** Gata-3 protein staining of spleen-derived T_{reg} cells (CD3⁺CD4⁺CD8⁻CD25⁺Foxp3⁺). Pseudocolor plots representative examples, quantification of Gata-3-positive cells ($n = 9-11$) and *Gata3* mRNA expression of sorted T_{reg} cells ($n = 4-5$) right (unpaired t -test). **i** Identification of T follicular regulatory cells in LN from WT vs. affected Δ/Δ animals. Tfr cells as CD3⁺CD4⁺CD8⁻CD25⁺Foxp3⁺Cxcr-5⁺PD-1⁺ T cells and quantified right ($n = 4$, unpaired t -test). **j** CD3⁺CD4⁺CD8⁻CD25⁺Foxp3⁺ T_{reg} cells from LN of WT or affected Δ/Δ animals co-stained with PD-1 and Gata-3. Percentage of Gata-3⁺PD-1⁺ T_{reg} cells quantified to the right ($n = 4$, unpaired t -test). Data are representative of two or more independent experiments with individual mice (**a, g, h**) or a single experiment with individual mice (**b, c, d-f, i-j**). Source data are provided as a Source Data file

to inhibit Gata-3 expression and T_{H2} polarization^{34,41}, including the expression of ST2⁴², and the Bach2–Batf interaction was shown to control T_{H2} -type immune responses⁴³. In addition, Bach2 supports the suppressive capacity of T_{reg} cells, as a loss-of-function study demonstrated that Bach2-deficient T_{reg} cells failed to prevent disease in a colitis model³⁴. *Dtx1*, previously reported to interact with Rbpj³², was also shown to be important for T_{reg} cell suppressive function in a transfer model of colitis³¹. Finally, the induction of ILT3 can lead to a severe defect in controlling T_{H2} -polarized immune responses via the induction of IRF4⁺PD-L2⁺ DCs³⁶.

This cumulative effect on T_{reg} suppressive capacity was finally leading to a loss of T_{H2} suppressive potential, a state where effector T_{H2} cells produced more IL-4, leading to even more Gata-3 expression in Δ/Δ T_{reg} cells. Gata-3 expression is required to maintain high Foxp3 expression levels and it is important to prevent T_{reg} differentiation into an effector phenotype⁴⁴⁻⁴⁶. But Gata-3 does not function in a binary on-off mode. It has been reported that Gata-3 over-expression in T cell progenitors changes the identity of developing double-negative thymocytes and drives them into the mast cell lineage⁴⁷⁻⁴⁹. These studies indicate that a well-defined Gata-3 dosage is required for proper T cell development and function. A recent report showed that the IL-4 signaling strength is important for T_{reg} cell function. By using mice carrying an IL-4Ra chain mutation leading to enhanced IL-4 signaling, the authors demonstrated that these T_{reg} cells, which were polarized towards a T_{H2} cell-like phenotype with high Gata-3 expression levels, had an impaired functionality⁵⁰.

Our data indicate that Rbpj could act as a Gata-3 dosage modifier, adjusting the balance of Gata-3 expression by restricting IL-4 sensitivity as a powerful molecular switch. In addition, published findings report that the *Gata3* gene itself is a direct target of Rbpj¹⁸. Therefore, the regulation of Gata-3 expression could be both on the transcriptional, as well as the IL-4 cytokine sensitivity level. Our findings should be considered in the current discussion that T_{H2} -polarized Gata-3⁺ T_{reg} cells are better suppressors of the corresponding T_{H2} -polarized effector T cells, a model proposed based on the complete deficiency of IRF4¹³. We could show that IL-4 and IL-33-induced Gata3^{high} T_{reg} cells express significantly more ILT3 upon in vitro expansion and differentiation, a surface receptor shown to interfere with efficient control of T_{H2} effector cells³⁶. Gata-3^{high} T_{reg} cells were unable to inhibit T_{H2} differentiation of IL-4 exposed naive CD4 cells in vitro. In contrast to this, they supported the maturation of a T_{H2} -promoting IRF4⁺PD-L2⁺ DC subpopulation in vitro.

Our motif analysis of the ATAC-sequencing data revealed a strong Gata signature in Δ/Δ T_{reg} -specific differentially accessible regions. Many of the affected genes were shared with $tisT_{reg}$ ST2 cells, a T_{H2} -biased T_{reg} subset normally present within non-lymphoid tissues⁷. Rbpj may regulate the Gata-3-dependent T_{reg} ST2 differentiation pathway and, thereby, might limit the access to the T_{reg} ST2 compartment in lymphoid organs to allow the maintenance of a diverse T_{reg} subset pool.

Methods

Mice. Wildtype C57BL/6, congenic B6.SJL-Ptprca^bPepc^b/BoyCrl (CD45.1⁺), and congenic B6.PL-Thy1³/Cj (CD90.1⁺) mice were obtained from Charles River Breeding Laboratories (Wilmington, MA, USA) or the Jackson Laboratory (Bar Harbor, ME, USA). B6N.129(Cg)-*Foxp3*^{tm3Ayr} mice (*Foxp3*.IRES-DTR/GFP)⁵¹ were bred to CD45.1⁺ or CD90.1⁺ mice in the animal facility of the German Cancer Research Center (DKFZ). B6.129(Cg)-*Foxp3*^{tm4(YFP/cre)Ayr/J}, Jackson (FOXP3.IRES-YFP/Cre)⁵² were crossed to Rbpj^{fl/fl} mice⁵³ to specifically delete Rbpj in T_{reg} cells. Age-matched littermate controls (Foxp3^{Cre}, YFP⁻ positive and wildtype for the Rbpj alleles) were used throughout the study. Details about hygiene status and barrier breeding conditions are explained in the following paragraph. Rag2-deficient (B6-Rag2tm1Fwa) lines were used to isolate protein for autoantibody detection. All animals were housed under specific pathogen-free conditions at the respective animal care facilities, and the governmental committee for animal experimentation (Regierungspräsidium Karlsruhe, Regierung von Unterfranken and Behörde für Gesundheit und Verbraucherschutz Hamburg) approved all experiments involving animals. Relevant ethical regulations for animal testing and research were complied with.

Breeding conditions and disease-free survival in barriers. Data from Fig. 1a are derived from animals housed under specified pathogen-free conditions in a specific mouse facility (called barrier 3) of the German Cancer Research Center, fulfilling the criteria given in the FELASA recommendations (animal number, health monitoring, age, agents, methods). All animals were housed in open cages allowing transmission of agents. Research personnel had access to the unit. Routine testing included testing for ectoparasites, endoparasites, bacteria and viruses. In barrier 3, murine norovirus (MNV), *Pneumocystis* sp. and *Staphylococcus aureus* have been detected, along with occasional detection of additional opportunistic agents. In our breeding, we observed 79 animals with T_{reg} lineage-specific bi-allelic *Rbpj* deletion (*Foxp3*^{Cre}*Rbpj*^{Δ/Δ}), of which 21 were sacrificed due to sickness and used for experimentation. Twenty-nine animals <20 weeks old were otherwise healthy but used for experimentation and censored for survival analysis. Thirty-two animals grew older than 20 weeks and were marked healthy during the observation period, although some turned sick later and were used for experimentation. Out of the 67 animals with mono-allelic *Rbpj* deletion (*Foxp3*^{Cre}*Rbpj*^{wt/Δ}) and 79 wildtype animals (*Foxp3*^{Cre}*Rbpj*^{wt/wt}), 0 animals showed signs of disease. All *Foxp3*^{Cre}*Rbpj*^{wt/Δ} and *Foxp3*^{Cre}*Rbpj*^{wt/wt} were littermates of the *Foxp3*^{Cre}*Rbpj*^{Δ/Δ} mice, housed in the same cages as their siblings.

To identify the influence of breeding conditions (and therefore the environmental influence) on disease development of *Foxp3*^{Cre}*Rbpj*^{Δ/Δ} animals, we transferred the colony to a newly established mouse facility (called barrier A) via embryo transfer (results in Fig. 4a). Mice in this barrier were colonized with a defined Altered Schaedler Flora and are housed in individually ventilated cages. Access is limited to animal caretaker personnel. Until study end, the barrier was completely free of infectious agents listed in the FELASA recommendations. In this barrier, we observed 55 animals with T_{reg} lineage-specific bi-allelic *Rbpj* deletion

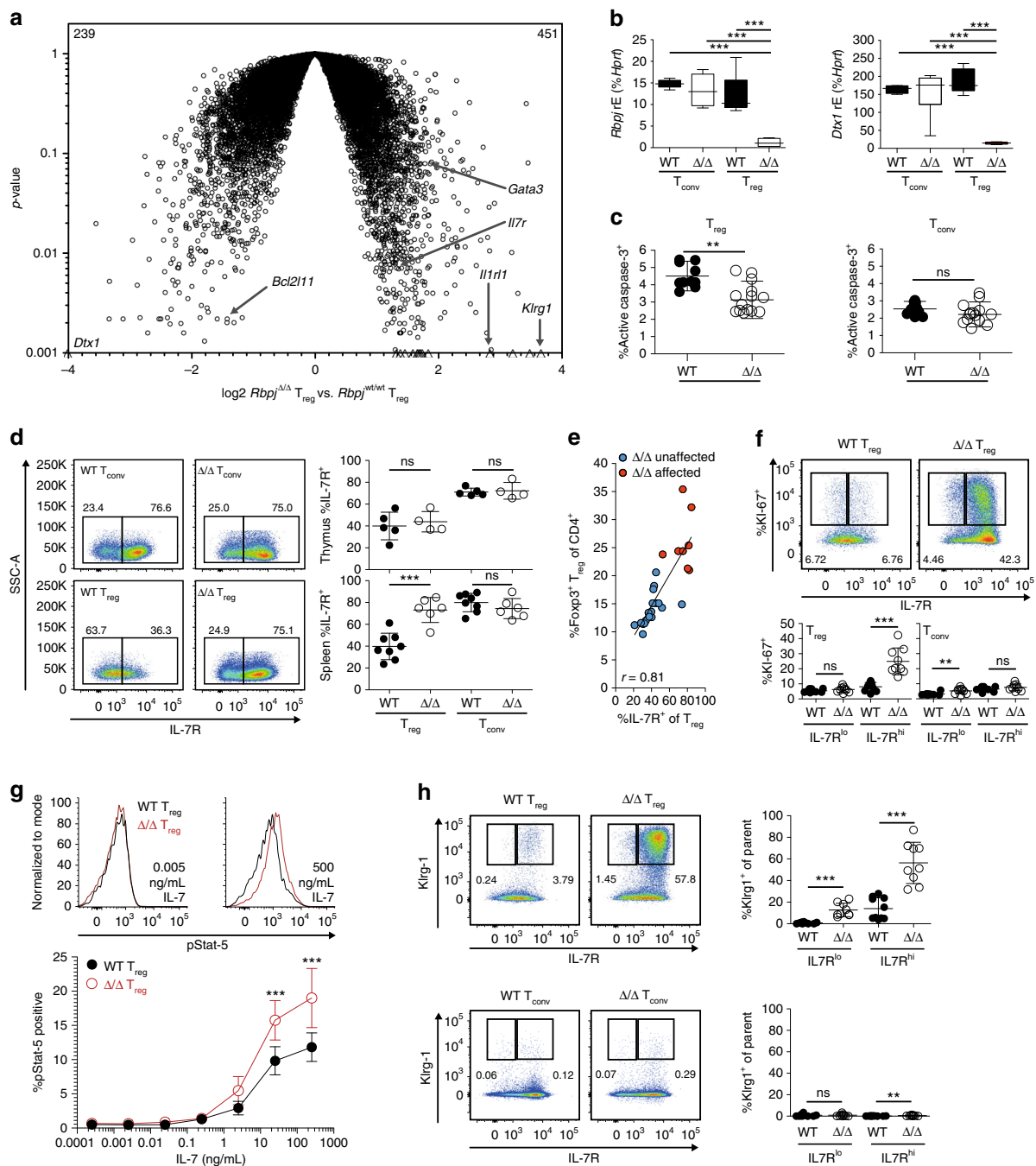


Fig. 6 Profiling of *Rbpj*-deficient T_{reg} cells. **a** Gene expression profile of T_{reg} cells (CD3⁺CD4⁺CD8⁻CD25⁺Foxp3⁺) from spleens of WT vs. affected Δ/Δ animals. Selected genes labeled. Average values of three biological replicates shown. Numbers show significantly up-regulated or under-represented genes in the comparison ($p < 0.05$). Statistical calculations described in Methods. Genes with p -values of < 0.001 set to 0.001 and labeled with a triangle.

b Measurement of *Rbpj* (left) and *Dtx1* (right) mRNA expression in FACS-isolated spleen-derived T_{reg} and T_{conv} cells from WT or unaffected Δ/Δ animals via Taqman qPCR ($n = 5-6$, one-way ANOVA with Newman-Keuls post-test). **c** Splenocytes isolated from WT and affected Δ/Δ animals treated with sulforhodamine-conjugated DEVD-FMK to label active caspase-3. T_{reg} or T_{conv} cells (CD3⁺CD4⁺CD8⁻CD25⁻Foxp3⁻) identified. Representative pseudocolor plots illustrating active Caspase-3 expression are shown in Supplementary Fig. 7. Statistical evaluation with unpaired t -test, $n = 10-14$. **d** Left panel, representative dot plots illustrating IL-7R expression on T_{conv} cells (upper panel) and T_{reg} cells (lower panel) found in WT (left) or affected Δ/Δ (right) animal-derived spleens; right panel, quantification ($n = 4-8$, unpaired t -test). **e** Correlation between frequency of IL-7R expression and frequency of T_{reg} cells. Values for healthy unaffected Δ/Δ animals (blue dots) and affected Δ/Δ animals (red dots) shown ($n = 17$ for blue dots, and $n = 8$ for red dots). R value displayed. **f** IL-7R and KI-67 expression in T_{reg} cells or T_{conv} cells derived from WT or affected Δ/Δ animals. Representative dot plots and quantification ($n = 9-10$, unpaired t -test). **g** Intracellular expression of phosphorylated Stat5 (pStat5) after IL-7 treatment of ex-vivo isolated splenocytes from WT vs. affected Δ/Δ animals. Representative histograms on top, percentage of intracellular pStat5 expression in T_{reg} cells below. Statistics based on two-way ANOVA with Bonferroni post-test ($n = 6$). **h** IL-7R and Klrp-1 expression in T_{reg} cells or T_{conv} cells from WT or affected Δ/Δ animals. Representative pseudocolor plots and quantification for T_{reg} and T_{conv} cells ($n = 8-10$, unpaired t -test). Data are representative of two or more independent experiments with individual mice (**b-f, h**) or a single experiment with several individual mice (**a, g**). Source data are provided as a Source Data file

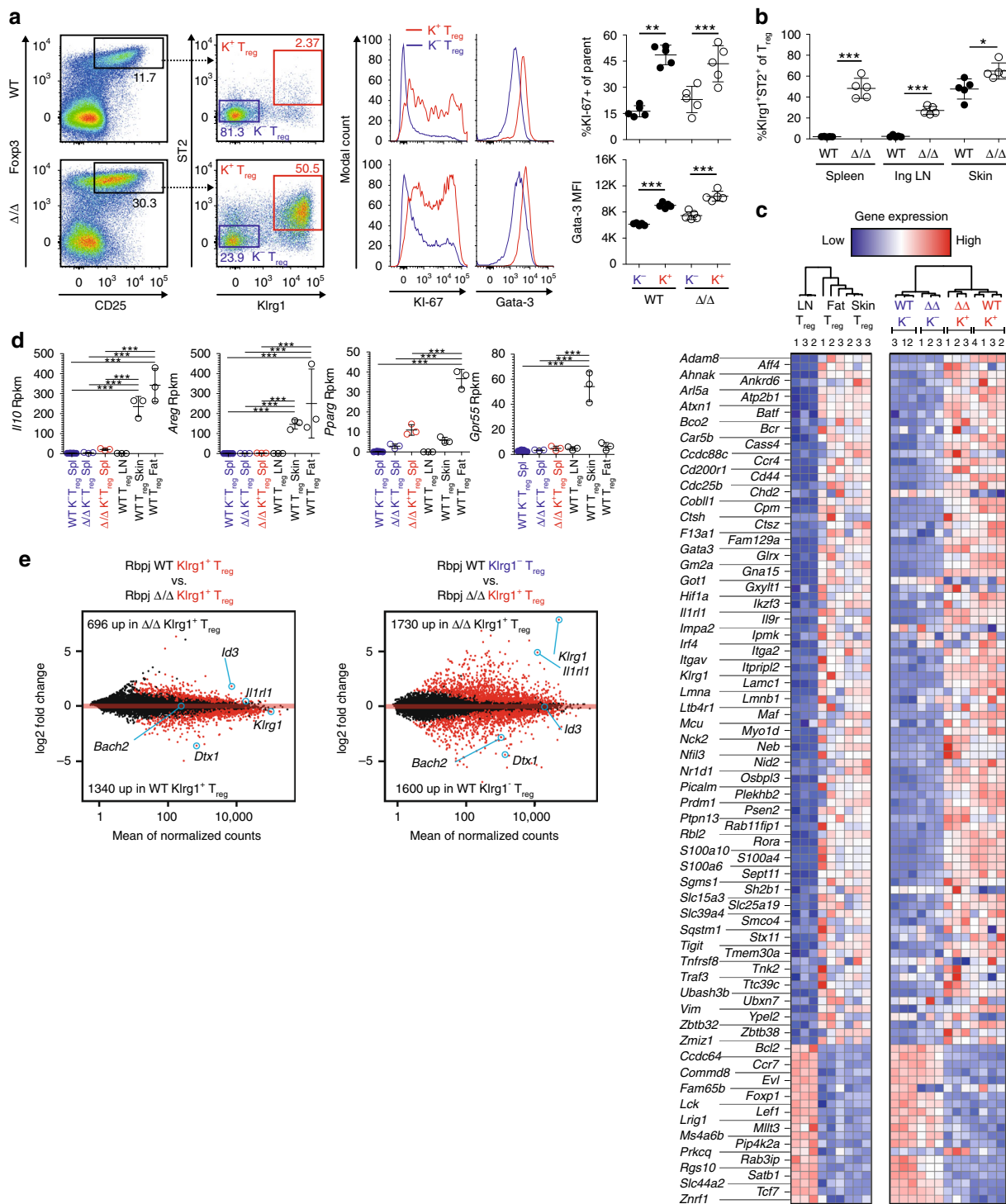
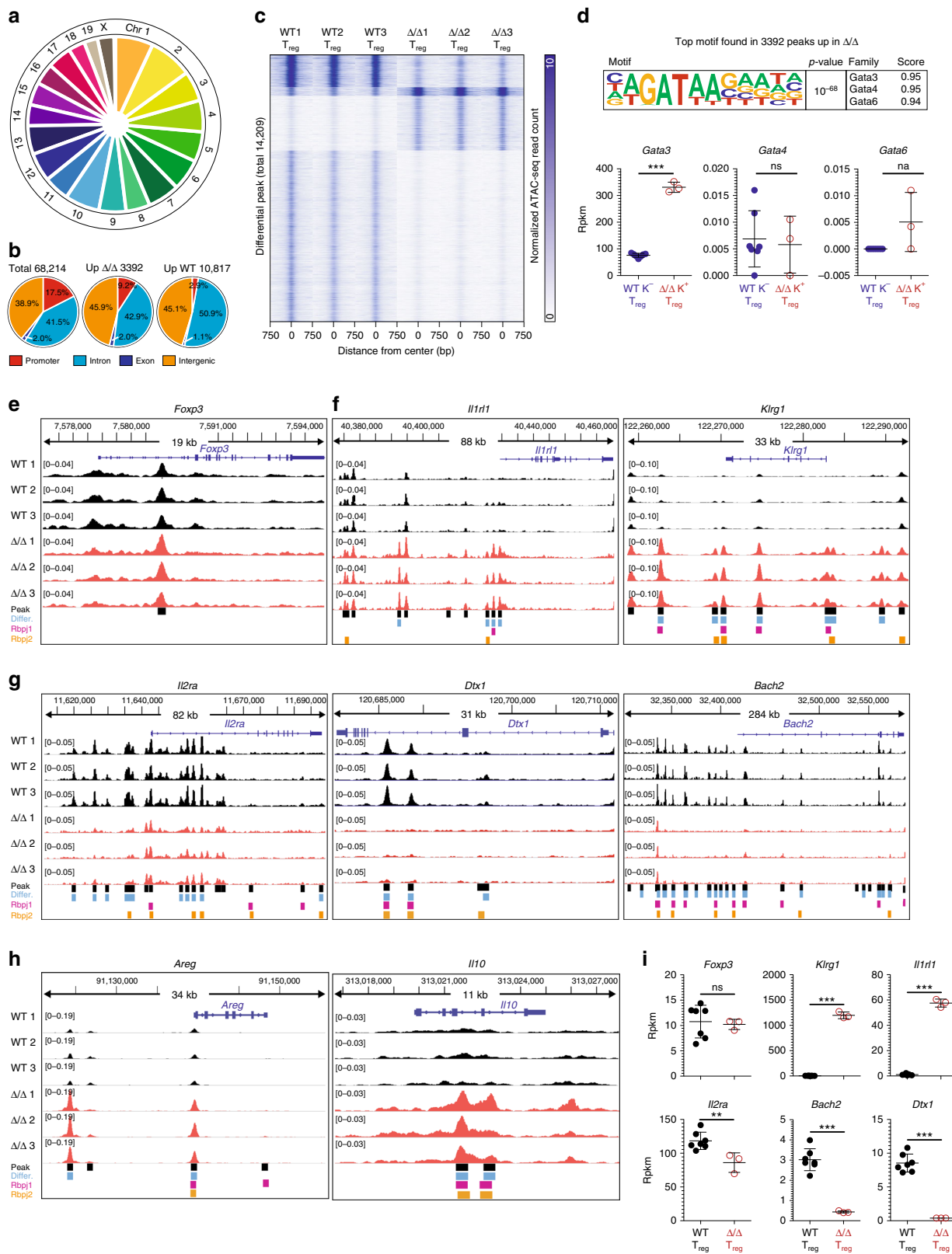


Fig. 7 Enrichment of ST2⁺Klrg1⁺ Treg cells in affected Δ/Δ animals. **a** T_{reg} cells (CD4⁺CD45⁺CD25⁺Foxp3⁺) identified in spleens from WT vs. affected Δ/Δ animals and sub-gated for presence of ST2⁺Klrg1⁺ tisT_{reg}ST2-like cells (representative pseudocolor plots to the left). Middle, histograms illustrating KI-67 and Gata-3 expression in ST2⁺Klrg1⁺ (K⁺) vs. ST2⁻Klrg1⁻ (K⁻) T_{reg} cells from WT and affected Δ/Δ animals, quantification to the right (n = 5, unpaired t-test). **b** Quantification of ST2⁺Klrg1⁺ T_{reg} cells in spleen, inguinal LN and skin of WT and affected Δ/Δ animals, (% of T_{reg}, n = 5, unpaired t-test). **c** RNA sequencing from spleen Δ/Δ Klrg1⁺ T_{reg} cells (Δ/Δ K⁺ T_{reg}, red), Δ/Δ Klrg1⁻ T_{reg} cells (Δ/Δ K⁻ T_{reg}, blue), WT Klrg1⁺ T_{reg} cells (WT K⁺ T_{reg}, red), and WT Klrg1⁻ T_{reg} cells (WT K⁻ T_{reg}, blue). Expression of 106 tisT_{reg}ST2 signature genes derived from a previous study⁷ in a heatmap with column dendrogram clustering. The expression of these signature genes in T_{reg} cells from fat, skin and LN T_{reg} cells shown to the left (Fat/Skin/LN WT T_{reg}). Heatmap and dendrogram created using R and heatmap function. **d** Expression of *Il10*, *Areg*, *Pparg*, and *Gpr55* in WT T_{reg} cells from skin, fat, or LN versus spleen (spl) Δ/Δ Klrg1⁺ T_{reg}, spleen Δ/Δ Klrg1⁻ T_{reg}, and spleen WT Klrg1⁻ T_{reg} cells. Statistical analysis of RNA-seq data described in Methods section. **e** MA plots illustrating expression of genes in two comparisons. Left, spleen WT Klrg1⁺ T_{reg} cells vs. spleen Δ/Δ Klrg1⁺ T_{reg} cells; right, spleen WT Klrg1⁻ T_{reg} cells vs. spleen Δ/Δ Klrg1⁺ T_{reg} cells. Individual genes are highlighted. Numbers indicate significantly expressed genes in the respective comparison. Data are representative of two or more independent experiments with individual mice (**a**, **b**) or a single experiment with several individual mice (**c-e**). Source data are provided as a Source Data file



(*Foxp3*^{Cre}*Rbpj* ^{Δ/Δ}), of which three were sacrificed due to sickness and used for experimentation. Seventeen animals <20 weeks old were otherwise healthy but used for experimentation and censored for survival analysis. Thirteen animals grew older than 20 weeks and were marked healthy during the observation period, although some turned sick later and were used for experimentation. Thirty-three animals were between 10 and 20 weeks old when the observation stopped and the experiment concluded. Out of the 45 animals with mono-allelic *Rbpj* deletion

(*Foxp3*^{Cre}*Rbpj*^{wt/ Δ}) and 40 wildtype animals (*Foxp3*^{Cre}*Rbpj*^{wt/wt}), 0 animals showed signs of disease.

Rbpj genotyping. Animal tails were digested in digest buffer (50 mM KCl, 20 mM Tris-HCl pH 8.8, 0.00045% Tween20 and Igepal CA-630) with proteinase K overnight at 56 °C. Following inactivation for 10 min at 96 °C, a PCR reaction with

Fig. 8 ATAC-seq of *Rbpj* Δ/Δ T_{reg} cells. **a** ATAC-seq with three biological replicates of Δ/Δ *Klrg1*⁺ T_{reg} cells and WT *Klrg1*⁻ T_{reg} cells. Identification of 68,214 peaks throughout the mouse genome. Distribution of all peaks across autosomes 1–19 and allosome x in a pie chart; pie size indicates contribution in percent. **b** Annotation of peaks to promoter (red), intron (light blue), exon (dark blue), or intergenic regions (orange). Left, annotation for all 68,214 peaks identified in the all dataset; middle, annotation for 3392 peaks specifically upregulated in Δ/Δ *Klrg1*⁺ T_{reg} cells; right, annotation for 10,816 peaks specifically upregulated in WT *Klrg1*⁻ T_{reg} cells. **c** Heatmap showing normalized ATAC-seq read counts in window of -750 bp to +750 bp around all differential peaks (14,208) for six samples. Y-axis individual peaks, X-axis distance from peak center. Color code indicates normalized ATAC-seq read count in 25 bp bins, with 0 = white and 10 = blue. **d** De novo motif analysis in 3392 peaks up in Δ/Δ T_{reg} cells. Top enriched de novo motif is shown, along with the corresponding *p*-value and the three most-similar known motifs (similarity score from 0 to 1, with 1 indicating an exact match). Further motifs and motif analysis for the 10,816 peaks up in WT shown in Supplementary Fig. 8a, b. Below, gene expression of *Gata3*, *Gata4*, and *Gata6* ($n = 3-7$, unpaired *t*-test). **e-h** ATAC-seq genome browser tracks for eight genes, with WT *Klrg1*⁻ T_{reg} cell data in black and Δ/Δ *Klrg1*⁺ T_{reg} cell data in red. Gene information is shown on top, along with the genomic location. Height indicates normalized ATAC-seq signal, the scale shown in brackets. All samples are group-normalized to allow peak height comparison. Below, all peaks (black squares), differential peaks (blue squares), instances of de novo *Rbpj*-binding motif (purple) or literature-based *Rbpj* motif (orange) are shown. Displayed are: *Foxp3* (**e**), *Il1rl1* and *Klrg1* (**f**), *Il2ra*, *Dtx1*, and *Bach2* (**g**), *Areg* and *Il10* (**h**). **i** RNA expression values (Rpkms) for genes shown in (**e-g**), data derived from RNA sequencing ($n = 3-7$, unpaired *t*-test). Data are representative of experiments with several individual mice. Source data are provided as a Source Data file

Taq polymerase, dNTPs, 2.5 mM MgCl₂, and 0.4 μ M *Rbpj* primers (GTGGAAC TTGCTATGTGCTTTG, CTGCCATATTGCTGAATGAAAA, CACATTCCCAT TATGATACTGAGTG) was started (95 °C, 5 min; 95°-30 s-58°-30 s-72°-30 s \times 35; 72 °C, 5 min). Samples were separated on an agarose gel and gene status analyzed. Similarly, *Foxp3*-driven presence of *Cre* recombinase was detected via PCR (AGGA TGTGAGGGACTACCTCCTGTA, TCCTTCACTCTGATTCTGGCAATTT; 94 °C, 3 min; 94°-40s-60°-40s-72°-60 s \times 30; 72 °C, 3 min).

Flow cytometry and fluorescence-activated cell sorting. Target organs were isolated and single-cell suspensions were established. If applicable, tissues were treated with collagenases and pre-purified according to protocol⁷. Red blood cells were lysed in hypotonic buffers, and cells were either pre-enriched with magnetic bead technology (Miltenyi Biotec) or directly stained with fluorochrome-labeled antibodies. Surface stainings were performed for 30 min at 4 °C, with all antibodies used at 1:100 dilution if not stated otherwise. If applicable, cells were fixed and afterwards permeabilized with the Foxp3 Fix/Perm Buffer set for 60 min at RT. Upon permeabilization, cells were stained intracellularly for 60 min at RT. Flow cytometry samples were acquired on a LSR II, Fortessa II or Canto II flow cytometer (BD Biosciences). For cell counting, AccuCheck counting beads were used (ThermoFisher). Samples for RNA isolation, DNA isolation, or subsequent cultivation were acquired and sorted on ARIA II or ARIA Fusion cell sorting systems (BD Biosciences) with four-way purity settings and an 85 μ m nozzle. For RNA collection, cells were sorted in 500 μ L of RNA lysis buffer, followed by RNA isolation based on manufacturer's instructions (RNEasy Mini Kit or RNEasy Micro Plus Kit, Qiagen). For DNA collection, samples were sorted into 500 μ L of DNA lysis buffer and DNA was purified according to manufacturer's protocol (DNEasy Blood and Tissue Kit, Qiagen). To harvest protein, cells were sorted into FCS-containing buffer and afterwards pelleted. Cells were lysed in RIPA buffer.

Real-time PCR. For RNA isolation, antibody-labeled cells were sorted directly into RT+lysis buffer and purified according to manufacturer's protocol (RNEasy mini Kit, Qiagen). RNA from whole tissues was isolated with mechanical tissue dissemination using ceramic beads followed by column-based RNA isolation (Innu-prep RNA Kit, Analytik Jena). RNA was reversely transcribed into cDNA according to manufacturer's protocol (Reverse Transcriptase II, life technologies). cDNA was used with Taqman probes and Taqman master mix or with Sybr primers and Sybr master mix in a Vii7 real-time PCR system (all ThermoFisher). Gene expression was normalized to housekeeping gene expression (*Hprt*) with the formula: relative gene expression = $2^{-Ct(\text{gene } X) - Ct(\text{Hprt})}$. Primer sequences and designations are listed in Supplementary Table 1.

Detection of *Rbpj* protein via Western Blot. T_{reg} (CD3⁺CD45⁺CD4⁺CD8⁻CD25⁺Foxp3-GFP⁺) and T_{conv} cells (CD3⁺CD45⁺CD4⁺CD8⁻CD25⁻Foxp3-GFP⁻) were isolated via FACS. Cells were lysed in RIPA buffer and supplemented with Laemmli buffer containing beta-mercaptoethanol. Samples were then heated to 95 °C for 10 min and afterwards separated by SDS-PAGE with pre-cast gels (Biorad). Gels were blotted onto PVDF membranes according to standard protocol. Membranes were blocked with 5% Milk-PBST for one hour at RT followed by incubation overnight with an anti-mouse *Rbpj* primary monoclonal antibody (Cell signaling clone D10A4) at 1:3000 in 5% Milk-PBST. Membranes were washed and RBPJ antibody was labeled with an HRP-conjugated secondary antibody at 1:10,000 dilution for one hour at RT. Membranes were washed and developed with a chromogenic detection reagent (Thermo Fisher).

Histology and microscopy. Immediately after the animals were sacrificed, organs were carefully excised and stored overnight in freshly prepared 4% formaldehyde solution. Afterwards, samples were embedded, thin-cut (thickness between 3 and 5 μ m) and stained. Haematoxylin and eosin (H&E) stainings, periodic acid-Schiff

reaction (PAS) stainings, and Giemsa stainings were prepared according to literature⁵⁴. Representative images were acquired on a Zeiss Axioplan microscope equipped with a AxioCam ICc 3 color camera with ZEN 2011 lite (BLUE EDITION) software. Intensity and contrast settings were adjusted for each organ but kept consistent between control and test sample. Foxp3-staining on embedded tissues was performed as follows: first, samples were thin-cut (3–5 μ m); second, paraffin was melted (72 °C, 30 min) followed by Xyloil (2 \times 5 min), and alcohol treatment; third, samples were incubated at 120 °C in Tris-EDTA buffer for 5 min, followed by blocking with peroxidase-block (Dako); then, incubation with primary antibody (Foxp3 FJK-16 s, 1:50, 30 min at RT) and secondary antibody (anti-rat HRP, 30 min at RT) with intermittent washing steps for 5 min (Washing buffer from Dako); last, chromogenic detection solution was added for 10 min at RT (DAB+ substrate, Dako) followed by 1 min incubation with Hematoxylin (Merck) and washing steps.

Immunohistochemistry and slide scanning/image analysis. Foxp3 stainings of embedded tissues were prepared with a fluorescence-labeled anti-Foxp3 antibody as described in literature⁵⁵. To visualize germinal centre formation, lymph node samples were recovered from animals, immediately frozen in TissueTec buffer (Sakura Finetek Europe) on cold carbon dioxide pellets and stored at -80 °C. Individual samples were cut from the tissue block and fixed with acetone for 10 min. Following blocking with 10% FCS, slides were incubated with AF488-labeled anti-mouse GL7 antibody (1:20), AF594-labeled anti-mouse IgD antibody (1:20), and AF 647-labeled anti-mouse CD4 antibody (1:20) overnight at 4 °C. After washing, samples were mounted with a fluorescent mounting medium (Dako). Unstained or single-stained samples were prepared and imaged as background staining controls. Samples were imaged on a motorized Zeiss inverted Cell Observer.Z1 with a mercury arc burner HXP 120/Colibri LED module, as well as a gray scale CCD camera AxioCam and a color CCD camera AxioCam MRC. Images were sequentially scanned and assembled with ZEN 2011 lite (BLUE EDITION) software. In order to obtain full-size images of lymph nodes, we first scanned the green channel (AF488, GL-7) followed by red channel (AF594, IgD), and blue channel (AF647, CD4). Contrast and fluorescence intensity were adjusted for all samples in parallel. To reduce robotic scanning errors, images were stitched to smooth transition areas. For Foxp3 stainings, staining intensity was normalized for each image.

Gene expression analysis with bead chips and statistics. For whole lymph-node gene expression analysis, inguinal lymph nodes from WT and affected Δ/Δ animals underwent mechanical tissue dissemination using ceramic beads followed by column-based RNA isolation, as described earlier. For gene expression analysis of T cells, we FACS-isolated spleen-derived T_{reg} (CD3⁺CD4⁺CD8⁻CD45⁺CD25⁺Foxp3-YFP⁺) and T_{conv} cells (CD3⁺CD4⁺CD8⁻CD45⁺CD25⁻Foxp3-YFP⁻) from WT and Δ/Δ animals. RNA was isolated (RNEasy mini kit) and the DKFZ Genomics and Proteomics Core Facility amplified and hybridized material to the Illumina MouseWG-6 v2.0 Expression BeadChip. Microarray scanning was done using an iScan array scanner. Data extraction was done for all beads individually, and outliers were removed when the absolute difference to the median was >2.5 times MAD (2.5 Hampelis method). Expression values were quantile normalized and log₂-transformed. Differentially expressed probes between groups were identified using the empirical Bayes approach based on moderated *t*-statistics as implemented in the Bioconductor package limma. All *p*-values in limma were adjusted for multiple testing using Benjamini-Hochberg correction in order to control the FDR. Probes with an FDR < 5% were considered statistically significant.

Statistical analysis of data. Data were analyzed with Prism software. We used a log-rank Mantel-Cox test in Kaplan-Meier survival curves (Figs. 1a and 4a), Mann-Whitney testing (Figs. 1b, c, d; 2b, c; 3a, b), unpaired *t* testing (Figs. 3d, e, f;

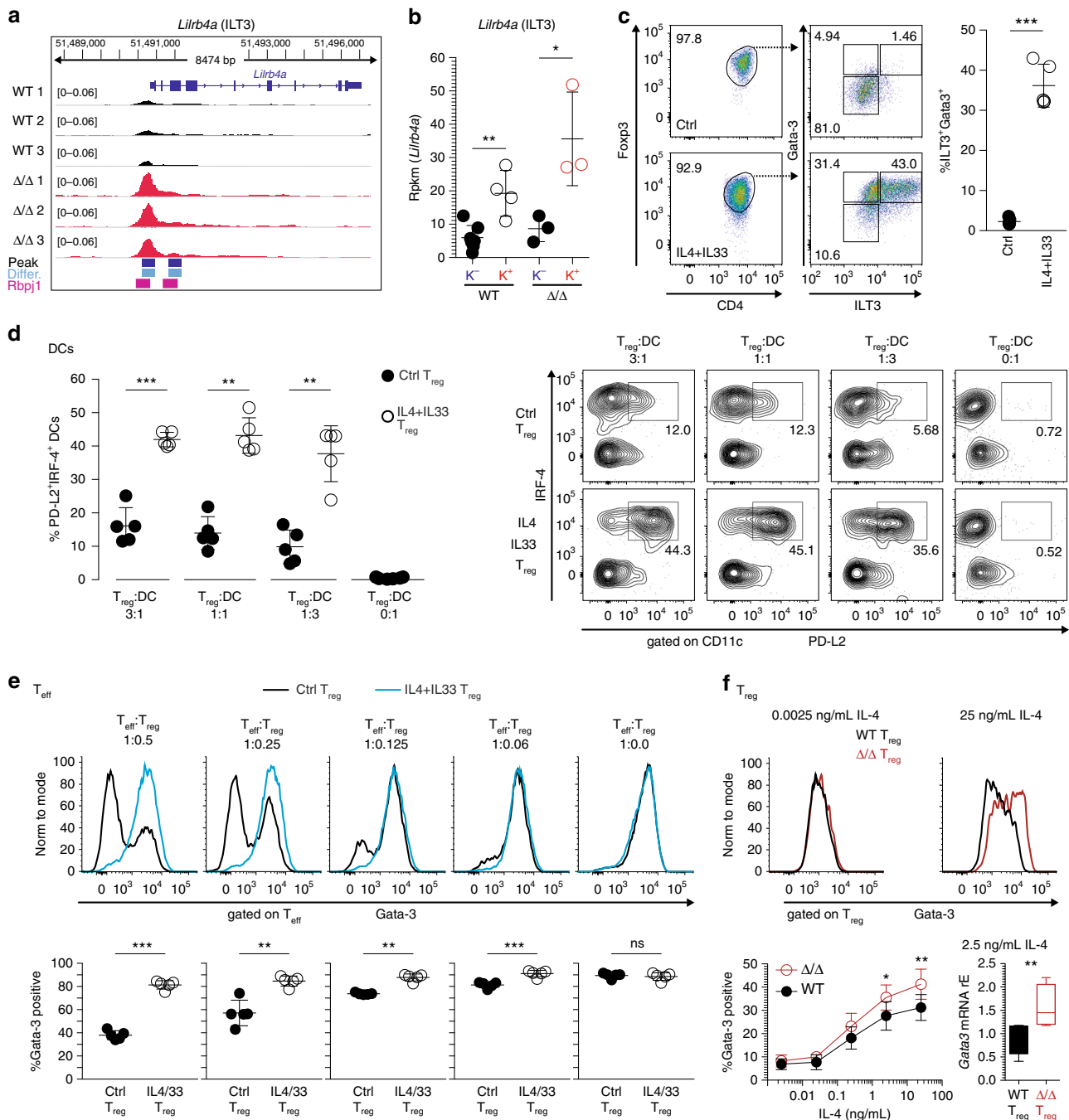


Fig. 9 ILT3⁺Gata3⁺ T_H2-biased T_{reg} cells fail to suppress T_H2 polarization. **a** ATAC-seq genome browser track for the *Lirb4a* gene (encoding for ILT3), with WT Klr1⁺T_{reg} cell data in black and Δ/Δ Klr1⁺ T_{reg} cell data in red. Gene information on top. Height indicates normalized ATAC-seq signal, scale shown in brackets. All samples group-normalized. Below, all peaks (black squares), differential peaks (blue squares), and de novo Rbpj-binding motif (purple). **b** *Lirb4a* gene expression based on RNA-seq data derived from WT and Δ/Δ Klr1⁻ and Klr1⁺ T_{reg} populations (*n* = 3–7, unpaired *t*-test). **c** WT T_{reg} cells (CD4⁺CD25⁺Foxp3-GFP⁺) expanded for 6 days in vitro with IL-4 and IL-33 (IL4+IL33 T_{reg} group) or without (control, Ctrl T_{reg} group). After 6 days, expression of FcγR3, Gata-3, and ILT3 measured by flow cytometry. Quantification right (*n* = 4, unpaired *t*-test). **d** 16-h DC polarization assay with different numbers of Gata-3-expressing T_{reg} cells or control T_{reg} cells (Ctrl T_{reg}) as in **c**. Expression of PD-L2 and IRF-4 in DCs (CD11c⁺MHCII⁺) measured by flow cytometry. Quantification left (paired *t*-test, *n* = 5) and representative dot plots right. **e** 96-h T-effector cell (T_{eff}) polarization assay with 20 ng/mL IL-4 and different numbers of either Gata-3-expressing T_{reg} cells (blue line) or control T_{reg} cells (black line) as in **c** and **d**, in the presence of DCs. Representative histograms showing Gata-3 expression in T_{eff} cells (CD4⁺CD11c⁺MHCII⁻CD25⁺Foxp3⁻) on top, quantification below (*n* = 5, paired *t*-test). **f** T_{reg} cells (CD4⁺CD25⁺Foxp3-YFP⁺) isolated from healthy, unaffected Δ/Δ and WT animals and stimulated with escalating doses of IL-4 followed by FACS measurement of Gata-3 protein. Representative histograms on top show Gata-3 expression in WT (black) or Δ/Δ (red) T_{reg} cells, treated with 0.0025 ng/mL IL-4 (left) or 25 ng/mL IL-4 (right). Below, Gata-3 expression across different doses. Statistics based on two-way ANOVA with Bonferroni post-test (*n* = 6). Lower right, qPCR-based verification of flow cytometry data for *Gata3* with 2.5 ng/mL IL-4 (*n* = 4, paired *t*-test). Data are representative of two or more independent experiments with individual mice (**c–f**) or a single experiment with several individual mice (**a, b**). Source data are provided as a Source Data file

4c, d, f, g, i, j; 5e, g–j; 6c, d, f, h; 7a, b; 8d, i; 9b, c, Supplementary Fig. 1a, c, d; Supplementary Fig. 2a), paired *t* testing (Figs. 4h and 9d–f), one-way ANOVA with Bonferroni post-testing (Figs. 5b and 6b; Supplementary Fig. 1b, Supplementary Fig. 2b) or Newmann–Keuls post-testing (Fig. 6b), or two-way ANOVA with Bonferroni post-testing (Figs. 6g and 9f, Supplementary Fig. 3). RNA-sequencing data in Figs. 2a, 6a and 7d, e were statistically evaluated as described in the respective paragraph of the Methods section. The respective number of animals (*n*) as well as the statistical test is also listed in the figure legend. All statistical test results and data used to calculate statistics are incorporated into the source data file.

Blood serum Ig subtype analysis. Blood was extracted via cardiac puncture from sacrificed animals and allowed to clot for at least 15 min. Afterwards, samples were centrifuged at 13,000 × *g* for 15 min and serum was collected. ELISA plates (Costar #9018) were pre-coated with goat-anti-mouse IgG + IgM (Dianova #115-005-0068) or goat-anti-mouse IgE (Biozol #1110-01) overnight at 4 °C, followed by washing and blocking (PBS 0.2% gelatine 0.1% NaN₃). Wells were incubated with serial dilutions of serum or control antibody for one hour at RT, followed by four washing steps. Peroxidase-conjugated secondary antibodies were added at 1:1000 dilution in PBS and incubated for one hour at RT, again followed by four washing steps. Plates were developed with 1 mg/mL OPD in 0.1 M KH₂PO₄ (pH 6.0) solution with 1 μL/mL of 30% H₂O₂ solution. Once colorimetric reaction was complete, incubation was stopped with 25 μL 1 M H₂SO₄ and read on a ELISA photometer at 490 nm wave length. All antibodies are listed in Supplementary Table 1.

Isolation of blood plasma and blood serum. Blood was collected from sacrificed mice via cardiac puncture. Blood was mixed with Heparin–PBS to a final concentration of 20 U/mL Heparin. Samples were centrifuged at 3000 × *g* for 15 min at 4 °C. Blood parameters were measured by photometric analysis on the ADVIA 2400 system (Siemens Healthcare Diagnostics) in the Zentrallabor (Medical Clinic-1, Analysezentrum) of the Heidelberg University Clinic. For blood serum collection, blood was extracted via cardiac puncture and allowed to clot for at least 15 min. Afterwards, samples were centrifuged at 13,000 × *g* for 15 min and blood serum was collected.

Autoantibody detection via Western Blot. Following organs and tissues from RAG2^{-/-} animals were isolated: brain, eye, spleen, lymph nodes, pancreas, salivary gland, stomach, liver, kidneys, heart, lung, testis, small, and large intestine. Tissues were weighted and adjusted to 100 mg, followed by addition of 500 μL ProteoJET mammalian cell lysis reagent (Fermentas) supplemented with 2X protease inhibitor (Roche Diagnostics). Tissues were mechanically dissected using scissors and incubated for 10 min at RT on an orbital shaker. Samples were then centrifuged for 15 min at 16,000 × *g* and supernatant containing protein lysate was harvested. Protein concentration was determined by BCA assay (Pierce). Twenty micrograms of protein were loaded per well on a pre-cast SDS gel (Biorad), followed by gel electrophoretic separation. Each gel contained eight wells with the same protein load (e.g. pancreas). After transfer on a PVDF membrane, this membrane was cut into eight strips containing the protein of interest. PVDF membranes were blocked with 5% Milk–PBST solution for one hour at RT following incubation with peripheral blood serum of individual mice (4 WT, 4 Δ/Δ) overnight at 4 °C (concentration 1:500 in 5% Milk–PBST). Individual strips were washed three times with PBST, followed by incubation with a HRP-conjugated donkey-anti-mouse IgG antibody (concentration 1:3000). After washing, strips were re-assembled and HRP activity was detected with a chromogenic substrate (Thermo Fisher).

Infection of WT and Δ/Δ animals with *S. ratti*. Animal experimentation was conducted at the animal facility of the Bernhard Nocht Institute for Tropical Medicine in agreement with the German animal protection law under the supervision of a veterinarian. The experimental protocols have been reviewed and approved by the responsible federal health authorities of the state of Hamburg, Germany, the Behörde für Gesundheit und Verbraucherschutz. Mice were sacrificed by cervical dislocation under deep CO₂ narcosis. Two cohorts with five WT and five healthy Δ/Δ animals each were infected on day 0 by injection of 1000 *S. ratti* larvae subcutaneously into the footpad. Cohort 1 was sacrificed 6 days after infection and intestinal parasite count, stool PCR, and flow cytometry (T_{reg} frequency, cytokine restimulation) were performed. Cohort 2 was sacrificed 14 days after infection; stool collection on day 6, 8, 10, 14 followed by stool-PCR; flow cytometry (T_{reg} frequency, cytokine restimulation) on day 14. To count the number of adult parasitic females in the gut, the small intestine was flushed slowly with tap water to remove feces, sliced open longitudinally and incubated at 37 °C for 3 h in a Petri dish with tap water. The released adult females were collected by centrifugation for 5 min at 1200 rpm and counted. To quantify the release of *S. ratti* larvae by infected mice, the feces of individual mice was collected over 24 h periods and DNA from representative 200 mg samples was extracted as described⁵⁶. Two hundred nanograms of DNA was used as a template for qPCR specific for *S. ratti* 28 S ribosomal RNA gene as described⁵⁷. For analysis of serum antibodies, blood was collected from infected mice at the indicated time points and allowed to coagulate for 1 h at RT. Serum was collected after centrifugation at 10,000 × *g* for 10

min at RT and stored at –20 °C for further analysis. *Strongyloides*-specific IgM in the serum was quantified by ELISA, as described⁵⁷. Serum concentration of IgE was quantified using the IgE ELISA kit according to the manufacturers recommendations. In flow cytometry experiments, spleens were collected, red blood cells lysed and samples stained as described previously. For cytokine restimulation experiments, single-cell suspensions were incubated with cell stimulation cocktail plus transport inhibitor for 6 h at 37 °C followed by intracellular cytokine staining. To measure secreted IL-9 levels, mesenteric LN-derived cells were mashed and incubated with anti-CD3 antibody (1 μg/mL) for 72 h at 37 °C with 1 × 10⁶ cells per well. IL-9 levels were quantified using the IL-9 ELISA kit according to the manufacturers recommendations.

Methylation of the TSDR. Genomic DNA of sorted cell populations was purified according to manufacturer's guidelines using the DNEasy Blood and Tissue kit (Quiagen). DNA purity and concentration were measured with a NanoDrop[®] photometer. Bisulfite-conversion was performed using the EpiTect Bisulfite Conversion Kit (Quiagen). Barcode-labeled primers for the *Foxp3* CNS2 (TSDR) were used to generate PCR amplicons from bisulfite-converted DNA (ForP: TGGGTT TTTTGGTATTTAAGAAAAG; RevP: AAAAAACAATAATCTACCCACAA). PCR amplicons were separated from primer dimers on a 2% agarose gel and purified using a Quick Gel Extraction Kit (Life Technologies). PCR amplicons were processed on a GS Junior Sequencer (Roche). Sequence reads were aligned to the BS-converted mouse genome and visualized.

In vitro T_{reg} suppression assay. First, we isolated MHCII-positive antigen-presenting cells (CD8⁻CD25⁻Foxp3-GFP⁻MHCII⁺CD90.1⁻CD90.2⁻) as well as CD4⁺ T-responder cells (CD4⁺CD8⁻CD25⁻Foxp3-GFP⁻MHCII⁻CD90.1⁺CD90.2⁻) from *Foxp3*^{GFP}, CD90.1 mice. T-responder cells were then labeled with carboxyfluorescein diacetate succinimidyl ester (CFSE) at 1 μM concentration in 10 mL cell culture medium for 15 min at RT, followed by several washing steps. Next, T_{reg} (CD4⁺CD8⁻CD25⁺Foxp3-YFP⁺MHCII⁻CD90.1⁻CD90.2⁺) and T_{conv} (CD4⁺CD8⁻CD25⁻Foxp3-YFP⁻MHCII⁻CD90.1⁻CD90.2⁺) cells from WT and affected Δ/Δ mice were isolated by FACS and serially diluted. In each well, 50,000 T-responder cells, 100,000 MHCII-positive APCs, and serially diluted T_{reg} or T_{conv} cells were added. To stimulate APC-driven T-responder cell proliferation, 2 μg/mL anti-CD3 antibody was added (Biolegend clone OKT3). Cells were incubated for 5 days at 37 °C, followed by re-staining for flow cytometric analysis of CFSE-dye dilution in T-responder cells.

TCR sequencing. Single cell suspensions from spleen and lymph nodes (combined axial, cervical, brachial) from individual WT vs. Δ/Δ mice were established, and red blood cells lysed. T_{reg} cells (CD3⁺CD4⁺CD8⁻CD45⁺CD25⁺Foxp3-YFP⁺) were pre-enriched with CD25-magnetic bead-based purification and sorted via FACS. Genomic DNA was isolated with the DNEasy blood and tissue kit according to manufacturer's instructions and measured on nanodrop photometer. Five hundred nanograms of gDNA per individual mouse were shipped to Adaptive Biotechnologies (Seattle, WA) for TCR sequencing. Data were analyzed with online tools provided by Adaptive Biotechnologies.

Active caspase-3 assay and intracellular cytokine secretion. For measurement of active caspase-3, single-cell suspensions were resuspended in FCS-containing cell culture medium (Gibco) and 1 μL of Red-DEVD-FMK (abcam) was added to each well in a 96-well tissue culture plate. Samples were incubated for 60 min at 37 °C, followed by washing with supplied wash buffer and surface antibody staining. As a positive control, splenocytes were incubated for 5 min at 42 °C. To measure intracellular cytokines, splenocytes, or lymph node-derived cell suspension were resuspended in FCS-containing cell culture medium. For stimulation, cells received 1X PMA-Ionomycin cocktail plus transport inhibitor, whereas controls received 1X transport inhibitor only cocktails (eBiosciences). Samples were incubated for 6–8 h at 37 °C, followed by surface and intracellular staining with Foxp3 Fix/perm staining mix.

Detection of phosphorylated Stat5 or Stat6. Spleen-derived single-cell suspensions were resuspended in FCS-containing cell culture medium (Gibco) and incubated at 37 °C in a 96-well tissue culture plate. Then, mouse recombinant IL-2, IL-4, or IL-7 were added in a 1+9 titration curve with a pre-warmed 2X mixture to cell suspension. Cells were incubated with the respective cytokine for 10 min at 37 °C. Afterwards, cells were centrifuged at 1000 × *g* and 4 °C for 2 min, followed by two washing steps with cold FACS buffer. Cells were fixed with 1X Fixation buffer (BD Fixation Buffer) for 30 min at 4 °C. Afterwards, cells were centrifuged and resuspended in –20 °C cooled Perm Buffer (BD PermBuffer III) and incubated for 30 min at 4 °C. Afterwards, cells were washed twice and stained with surface and intracellular antibodies for 30 min at 4 °C, followed by analysis via flow cytometry.

RNA sequencing. cDNA was generated and amplified using 4.8 ng of total RNA (RNeasy Mini Kit) and SMARTer Ultra Low Input RNA for Illumina Sequencing –HV (Clontech Laboratories, Inc.) according to the manufacturer's protocol. Then, sequencing libraries were prepared using the NEXT ChIP-Seq Library Prep Master Mix Set for Illumina (New England Biolabs) according to the

manufacturer's instructions with the following modifications: The adapter-ligated double-stranded cDNA (10 μ L) was amplified using NEBNext Multiplex Oligos for Illumina (New England Biolabs, 25 μ M primers), NEBNext High-Fidelity 2x PCR Master Mix (New England Biolabs) and 15 cycles of PCR. Final libraries were validated using Agilent 2100 Bioanalyzer (Agilent Technologies) and Qubit fluorometer (Invitrogen), normalized and pooled in equimolar ratios. 50 bp single-read sequencing was performed on the Illumina HiSeq 2000 v4 according to the manufacturer's protocol.

Mapping of RNA seq data, statistical evaluation, and plotting. For all samples, low-quality bases were removed with `Fastq_quality_filter` from the FASTX Toolkit 0.0.13 (http://hannonlab.cshl.edu/fastx_toolkit/index.html) with 90% of the read needing a quality phred score >20. `Homertools 4.7`⁵⁸ were used for PolyA-tail trimming, and reads with a length <17 were removed. `PicardTools 1.78` (<https://broadinstitute.github.io/picard/>) were used to compute the quality metrics with `CollectRNASeqMetrics`. With `STAR 2.3`⁵⁹, the filtered reads were mapped against mouse genome 38 using default parameters. Count data and RPKM tables were generated by mapping filtered reads against union transcripts (derived from Mouse Ensembl 90) using a custom pipeline. Mapping was carried out with `bowtie2` version 2.2.4⁶⁰ against union mouse genes: every gene is represented by a union of all its transcripts (exons). The count values (RPKM and raw counts) were calculated by running `CoverageBed` from `Bedtools v2.26.0`⁶¹ of the mapped reads together with the mouse annotation file (Ensembl 90) in `gff` format and parsing the output with custom perl scripts. The input tables containing the replicates for groups to compare were created by a custom perl script. For `DESeq2`⁶², `DESeqDataSetFromMatrix` was applied, followed by `estimateSizeFactors`, `estimateDispersions`, and `nbinomWald` testing. The result tables were annotated with gene information (gene symbol, gene type) derived from the `gencode.vM16.annotation.gtf` file. The results were then filtered for protein-coding genes according to the `gencode.vM16.annotation.gtf` file. To account for the gender differences between male and female mice, 4571 differently expressed genes with an *adj. p*-value < 0.05 in the comparison of wildtype spleen-derived `TCR β +CD4+CD8-CD25+Foxp3-` (GFP)+`Klrg1-ST2-` (female) with wildtype spleen-derived `TCR β +CD4+CD8-CD25+Foxp3(GFP)+Klrg1-ST2-` (male) cells were excluded from the input tables into `DESeq2` and the analyses were rerun with the remaining genes. MA plots were generated as described in ref. ⁶³. PCA plots and tables were generated using the `plotPCA` function of `DESeq2` for the most variable 500 genes after applying the `DESeq2` `varianceStabilizingTransformation` to the data.

ATAC-seq. The assay for transposase-accessible chromatin using sequencing (ATAC-seq) was performed according to Buenrostro et al. ³⁵ with some modifications. In brief, about 50,000 FACS-isolated cells were pelleted on with 10,000 \times g for 3 min and supernatant removed. Cells were tagged at 55 $^{\circ}$ C for 8 min in 50 μ L 1x tagmentation buffer including 2.5 μ L transposome from the Nextera DNA library prep kit and 0.01% digitonin. The transposome was inactivated by addition of 20 μ L 5 M guanidinium thiocyanate, and the DNA was purified with two volumes, i.e., 140 μ L, of DNA-binding beads (HighPrep beads). The DNA was PCR amplified with a `LightCycler 480` (Roche) in a 50 μ L reaction with the NEBNext High Fidelity mix including 0.5 μ L 1x SYBRGreen, forward primer `Tn5Mcp1n` (AATGATACGGCGACCCAGAGATCTACACTCGTCGGCAGCGTC) and barcoded reverse primers `Tn5mCbar` (CAAGCAGAAGACGGCAGATACGAGAT (8–9N barcode) GTCTCGTGGGCTCGG); 72 $^{\circ}$ C, 5 min; 98 $^{\circ}$ C, 30 s (gap repair and initial melting); then cycling with 98 $^{\circ}$ C, 10 s; 63 $^{\circ}$ C, 30 s; 72 $^{\circ}$ C, 30 s for 15 cycles when all amplifications turned into saturation. PCR products were purified with 1.4 volumes (70 μ L) magnetic beads. Ten microliters of eluates were sequenced on a HiSeq2000, 125 bp paired-end.

ATAC-seq data analysis. ATAC-seq read data were processed as described previously⁶⁴. Reads were trimmed using `Skewer`⁶⁵ and aligned to the mm10 assembly of the murine genome using `Bowtie2`⁶⁰ with the '-very-sensitive' parameter. Duplicate reads were removed using `sambamba markdup`⁶⁶, and only properly paired reads with mapping quality >30 were kept. Reads were shifted as previously described to account for the transposition event³⁵. Bigwig files were created using `bedtools`⁶¹. Preprocessed ATAC-seq data was analyzed with the `HOMER` package⁵⁸. In brief, mapped sequencing reads were transformed to tag directories using the option '-sensitivity 3'. Peaks were called on all reads in all samples using the 'findPeaks' command with the options '-style factor -size 350 -minDist 300 -L 2'. Peaks from the mitochondrial genome and ENCODE blacklisted regions⁶⁷ were removed. Based on this consensus peak set, differential peaks were called using the `DESeq2` implementation of `HOMER`. Specifically, reads from all individual experiments were counted in all individual peaks of consensus peak set using the 'annotatePeaks.pl' command with the option '-raw'. Based on the read count at each peak, significantly differential peaks were called using the 'getDiffExpression.pl' command using the '-norm2total' option. Motifs were then called on differential peaks using the 'findMotifsGenome.pl' command using the 'hypergeometric' option for *p*-value calculations. As a background, the non-differential peak set was used. The final motif sets were filtered for motifs with a significance <1e-10 and with an occurrence of <0.5% in the background regions set in case the non-differential peaks were used as a background file for motif finding using the

'compareMotifs.pl' command. To create heatmaps of differential peaks, sequencing reads were annotated to the differential peaks in 25 bp bins in a region of -750 bp to +750 bp from the peak center. The data matrix was clustered using `Cluster 3.0`⁶⁸ with the *k*-means option, and the heatmap was visualized with the `TreeView 3`⁶⁹ software.

In-vitro T_{reg} differentiation with IL-4 and IL-33. Spleen and lymph-nodes were isolated and single-cell suspensions established. T_{reg} cells were pre-purified using CD25-based magnetic bead staining and column-based isolation, followed by FACS-based sorting of `CD4+CD25+Foxp3-GFP+` T_{reg} cells. 20,000 cells each were supplemented with either recombinant mouse IL-4 (500 ng/mL) plus recombinant mouse IL-33 (500 ng/mL) (IL4 + IL33 T_{reg} group) or without additional cytokines (Ctrl T_{reg} group). In addition, both T_{reg} groups were cultured with 5000 U/mL IL-2 and anti-CD3/28 microbeads at 4:1 bead to cell ratio were added to each well. Cells were incubated with the respective cytokine mix for 6 days at 37 $^{\circ}$ C, medium was re-supplemented on day 4. On day 6, cells were counted using a flow cytometer and expression of ILT3 and Gata-3 was measured. Cells were washed three times to remove remaining cytokines and used for the in vitro DC differentiation assay and for the in vitro T_{eff} polarization assay.

In vitro DC differentiation assay. Spleen and mesenteric LNs from donor animals were isolated and single-cell suspensions established. DCs were pre-purified using `CD11c` microbeads and column-based isolation, followed by FACS-based sorting of a `MCHII+CD11c+` population. DCs were stimulated with LPS (100 ng/mL), and anti-CD3 (4 μ g/mL) was added. In vitro expanded T_{reg} cells were added at indicated ratios (APC:T_{reg} 1:3, 1:1, 3:1, 1:0) and incubated for 16 h at 37 $^{\circ}$ C. Cells were fixed, and DCs were analyzed after antibody surface and intracellular staining with the BD Fix/Perm Buffer kit.

In vitro T_{eff} polarization assay. Spleen and mesenteric LNs from donor animals were isolated and single-cell suspensions established. T_{eff} cells were pre-purified using CD4 microbeads and column-based isolation, followed by FACS-based sorting of `CD4+CD25-Foxp3-GFP-CD62L+` naive T_{eff} cells. 5 \times 10⁴-purified T_{eff} cells were co-cultured with expanded T_{reg} cells at various ratios (T_{eff}:T_{reg} 1:0.5, 1:0.25, 1:0.125, 1:0.06, 1:0) and 1 \times 10⁴ FACS-sorted DCs (`MCHII+CD11c+`). Anti-CD3 (4 μ g/mL) and recombinant mouse IL-4 (20 ng/mL), as well as mouse IFN γ -blocking mAb (20 μ g/mL) were added and cells were incubated for 96 h at 37 $^{\circ}$ C. Cells were fixed, followed by surface and intracellular staining with the `Foxp3 Fix/Perm Buffer kit`.

Measurement of Gata-3 induction upon cytokine challenge. Spleen and lymph-node-derived T_{reg} cells (`CD4+CD8-CD25+Foxp3-YFP+`) were isolated from WT and healthy Δ/Δ animals via FACS. 75,000 cells each were supplemented with IL-4 at different concentrations, along with 5000 U/mL IL-2, 20 μ g/mL IL-12 blocking mAb, 20 μ g/mL IFN γ -blocking antibody, and CD3/CD28 microbeads at 4:1 bead to cell ratio. Cells were incubated with the respective cytokine for 40 h at 37 $^{\circ}$ C, followed by surface and intracellular staining with the `Foxp3 Fix/Perm Buffer kit`.

Reporting summary. Further information on experimental design is available in the Nature Research Reporting Summary linked to this article.

Data availability

RNA microarray data, RNA sequencing data and ATAC-sequencing data that support the findings of the study have been deposited in the Gene Expression Omnibus (<https://www.ncbi.nlm.nih.gov/geo/query/acc.cgi>) under the accession number GSE119169. The source data underlying Figs. 1a–d, 2a–c, 3a, b, 3d–f, 4a, c, d, f–j, 5b, d–e, g–j, 6a–h, 7a–d, 8a–d, i, 9b–f, and Supplementary Figs. 1–4 and 8a, b are provided as a Source Data file. All other data are available from the author upon reasonable request.

Received: 13 April 2018 Accepted: 26 February 2019

Published online: 08 April 2019

References

- Wildin, R. S. et al. X-linked neonatal diabetes mellitus, enteropathy and endocrinopathy syndrome is the human equivalent of mouse scurfy. *Nat. Genet.* **27**, 18–20 (2001).
- Brunkow, M. E. et al. Disruption of a new forkhead/winged-helix protein, scurfy, results in the fatal lymphoproliferative disorder of the scurfy mouse. *Nat. Genet.* **27**, 68–73 (2001).
- Khattry, R., Cox, T., Yasayko, S. A. & Ramsdell, F. An essential role for Scurfin in CD4⁺ CD25⁺ T regulatory cells. *Nat. Immunol.* **4**, 337–342 (2003).
- Hori, S., Nomura, T. & Sakaguchi, S. Control of regulatory T cell development by the transcription factor Foxp3. *Science* **299**, 1057–1061 (2003).

5. Fontenot, J. D., Gavin, M. A. & Rudensky, A. Y. Foxp3 programs the development and function of CD4+ CD25+ regulatory T cells. *Nat. Immunol.* **4**, 330–336 (2003).
6. Ohkura, N. et al. T cell receptor stimulation-induced epigenetic changes and Foxp3 expression are independent and complementary events required for Treg cell development. *Immunity* **37**, 785–799 (2012).
7. Delacher, M. et al. Genome-wide DNA-methylation landscape defines specialization of regulatory T cells in tissues. *Nat. Immunol.* **18**, 1160–1172 (2017).
8. Kitagawa, Y. et al. Guidance of regulatory T cell development by Satb1-dependent super-enhancer establishment. *Nat. Immunol.* **18**, 173–183 (2017).
9. Schmidl, C. et al. Lineage-specific DNA methylation in T cells correlates with histone methylation and enhancer activity. *Genome Res.* **19**, 1165–1174 (2009).
10. Feuerer, M. et al. Lean, but not obese, fat is enriched for a unique population of regulatory T cells that affect metabolic parameters. *Nat. Med.* **15**, 930–939 (2009).
11. Campbell, D. J. & Koch, M. A. Phenotypical and functional specialization of FOXP3+ regulatory T cells. *Nat. Rev. Immunol.* **11**, 119–130 (2011).
12. Koch, M. A. et al. The transcription factor T-bet controls regulatory T cell homeostasis and function during type 1 inflammation. *Nat. Immunol.* **10**, 595–602 (2009).
13. Zheng, Y. et al. Regulatory T-cell suppressor program co-opts transcription factor IRF4 to control T(H)2 responses. *Nature* **458**, 351–356 (2009).
14. Chaudhry, A. et al. CD4+ regulatory T cells control TH17 responses in a Stat3-dependent manner. *Science* **326**, 986–991 (2009).
15. Radtke, F., Fasnacht, N. & Macdonald, H. R. Notch signaling in the immune system. *Immunity* **32**, 14–27 (2010).
16. Tu, L. et al. Notch signaling is an important regulator of type 2 immunity. *J. Exp. Med.* **202**, 1037–1042 (2005).
17. Amsen, D., Antov, A. & Flavell, R. A. The different faces of Notch in T-helper-cell differentiation. *Nat. Rev. Immunol.* **9**, 116–124 (2009).
18. Amsen, D. et al. Direct regulation of Gata3 expression determines the T helper differentiation potential of Notch. *Immunity* **27**, 89–99 (2007).
19. Fang, T. C. et al. Notch directly regulates Gata3 expression during T helper 2 cell differentiation. *Immunity* **27**, 100–110 (2007).
20. Charbonnier, L. M., Wang, S., Georgiev, P., Sefik, E. & Chatila, T. A. Control of peripheral tolerance by regulatory T cell-intrinsic Notch signaling. *Nat. Immunol.* **16**, 1162–1173 (2015).
21. Stavnezer, J. Immunoglobulin class switching. *Curr. Opin. Immunol.* **8**, 199–205 (1996).
22. Breloer, M. & Abraham, D. Strongyloides infection in rodents: immune response and immune regulation. *Parasitology* **144**, 295–315 (2017).
23. Reitz, M. et al. Mucosal mast cells are indispensable for timely termination of *Strongyloides ratti* infection. *Mucosal Immunology* **10**, 481–492 (2017).
24. Blankenhaus, B. et al. Foxp3(+) regulatory T cells delay expulsion of intestinal nematodes by suppression of IL-9-driven mast cell activation in BALB/c but not in C57BL/6 mice. *PLoS Pathog.* **10**, e1003913 (2014).
25. Polansky, J. K. et al. DNA methylation controls Foxp3 gene expression. *Eur. J. Immunol.* **38**, 1654–1663 (2008).
26. Concannon, C. G. et al. AMP kinase-mediated activation of the BH3-only protein Bim couples energy depletion to stress-induced apoptosis. *J. Cell Biol.* **189**, 83–94 (2010).
27. Kilbride, S. M. et al. AMP-activated protein kinase mediates apoptosis in response to bioenergetic stress through activation of the pro-apoptotic Bcl-2 homology domain-3-only protein BMF. *J. Biol. Chem.* **285**, 36199–36206 (2010).
28. Surh, C. D. & Sprent, J. Homeostasis of naive and memory T cells. *Immunity* **29**, 848–862 (2008).
29. Soares, A. et al. Novel application of Ki67 to quantify antigen-specific in vitro lymphoproliferation. *J. Immunol. Methods* **362**, 43–50 (2010).
30. Foxwell, B. M., Beadling, C., Guschin, D., Kerr, I. & Cantrell, D. Interleukin-7 can induce the activation of Jak 1, Jak 3 and STAT 5 proteins in murine T cells. *Eur. J. Immunol.* **25**, 3041–3046 (1995).
31. Hsiao, H. W. et al. Deltex1 antagonizes HIF-1 α and sustains the stability of regulatory T cells in vivo. *Nat. Commun.* **6**, 6353 (2015).
32. Yamamoto, N. et al. Role of Deltex-1 as a transcriptional regulator downstream of the Notch receptor. *J. Biol. Chem.* **276**, 45031–45040 (2001).
33. Miyazaki, M. et al. Id2 and Id3 maintain the regulatory T cell pool to suppress inflammatory disease. *Nat. Immunol.* **15**, 767–776 (2014).
34. Roychoudhuri, R. et al. BACH2 represses effector programs to stabilize T (reg)-mediated immune homeostasis. *Nature* **498**, 506–510 (2013).
35. Buenrostro, J. D., Giresi, P. G., Zaba, L. C., Chang, H. Y. & Greenleaf, W. J. Transposition of native chromatin for fast and sensitive epigenomic profiling of open chromatin, DNA-binding proteins and nucleosome position. *Nat. Methods* **10**, 1213–1218 (2013).
36. Ulges, A. et al. Protein kinase CK2 enables regulatory T cells to suppress excessive TH2 responses in vivo. *Nat. Immunol.* **16**, 267–275 (2015).
37. Williams, J. W. et al. Transcription factor IRF4 drives dendritic cells to promote Th2 differentiation. *Nat. Commun.* **4**, 2990 (2013).
38. Gao, Y. et al. Control of T helper 2 responses by transcription factor IRF4-dependent dendritic cells. *Immunity* **39**, 722–732 (2013).
39. Wang, H. et al. NOTCH1-RBP complexes drive target gene expression through dynamic interactions with superenhancers. *Proc. Natl Acad. Sci. USA* **111**, 705–710 (2014).
40. Furtado, G. C., Curotto de Lafaille, M. A., Kutchukhidze, N. & Lafaille, J. J. Interleukin 2 signaling is required for CD4(+) regulatory T cell function. *J. Exp. Med.* **196**, 851–857 (2002).
41. Kim, E. H. et al. Bach2 regulates homeostasis of Foxp3+ regulatory T cells and protects against fatal lung disease in mice. *J. Immunol.* **192**, 985–995 (2014).
42. Tsukumo, S. et al. Bach2 maintains T cells in a naive state by suppressing effector memory-related genes. *Proc. Natl Acad. Sci. USA* **110**, 10735–10740 (2013).
43. Kuwahara, M. et al. Bach2-Batf interactions control Th2-type immune response by regulating the IL-4 amplification loop. *Nat. Commun.* **7**, 12596 (2016).
44. Yu, F., Sharma, S., Edwards, J., Feigenbaum, L. & Zhu, J. Dynamic expression of transcription factors T-bet and GATA-3 by regulatory T cells maintains immunotolerance. *Nat. Immunol.* **16**, 197–206 (2015).
45. Wang, Y., Su, M. A. & Wan, Y. Y. An essential role of the transcription factor GATA-3 for the function of regulatory T cells. *Immunity* **35**, 337–348 (2011).
46. Wohlfert, E. A. et al. GATA3 controls Foxp3(+) regulatory T cell fate during inflammation in mice. *J. Clin. Invest.* **121**, 4503–4515 (2011).
47. Tagnon, T. et al. Enforced expression of GATA-3 severely reduces human thymic cellularity. *J. Immunol.* **167**, 4468–4475 (2001).
48. Scripture-Adams, D. D. et al. GATA-3 dose-dependent checkpoints in early T cell commitment. *J. Immunol.* **193**, 3470–3491 (2014).
49. Tagnon, T., Yui, M. A. & Rothenberg, E. V. Mast cell lineage diversion of T lineage precursors by the essential T cell transcription factor GATA-3. *Nat. Immunol.* **8**, 845–855 (2007).
50. Noval Rivas, M. et al. Regulatory T cell reprogramming toward a Th2-cell-like lineage impairs oral tolerance and promotes food allergy. *Immunity* **42**, 512–523 (2015).
51. Kim, J. M., Rasmussen, J. P. & Rudensky, A. Y. Regulatory T cells prevent catastrophic autoimmunity throughout the lifespan of mice. *Nat. Immunol.* **8**, 191–197 (2007).
52. Rubtsov, Y. P. et al. Regulatory T cell-derived interleukin-10 limits inflammation at environmental interfaces. *Immunity* **28**, 546–558 (2008).
53. Nakhai, H. et al. Conditional ablation of Notch signaling in pancreatic development. *Development* **135**, 2757–2765 (2008).
54. Romeis. *Mikroskopische Technik*, Vol. 19 (Springer Spektrum, Berlin, Heidelberg, 2015).
55. Federico, G. et al. Tubular Dickkopf-3 promotes the development of renal atrophy and fibrosis. *JCI Insight* **1**, e84916 (2016).
56. Nour, N. B. et al. Vaccination with *Strongyloides ratti* heat shock protein 60 increases susceptibility to challenge infection by induction of Th1 response. *Vaccine* **30**, 862–871 (2012).
57. Eschbach, M. L. et al. *Strongyloides ratti* infection induces transient nematode-specific Th2 response and reciprocal suppression of IFN- γ production in mice. *Parasite Immunol.* **32**, 370–383 (2010).
58. Heinz, S. et al. Simple combinations of lineage-determining transcription factors prime cis-regulatory elements required for macrophage and B cell identities. *Mol. Cell* **38**, 576–589 (2010).
59. Dobin, A. et al. STAR: ultrafast universal RNA-seq aligner. *Bioinformatics* **29**, 15–21 (2013).
60. Langmead, B. & Salzberg, S. L. Fast gapped-read alignment with Bowtie 2. *Nat. Methods* **9**, 357–359 (2012).
61. Quinlan, A. R. & Hall, I. M. BEDTools: a flexible suite of utilities for comparing genomic features. *Bioinformatics* **26**, 841–842 (2010).
62. Anders, S. & Huber, W. Differential expression analysis for sequence count data. *Genome Biol.* **11**, R106 (2010).
63. Anders, S. et al. Count-based differential expression analysis of RNA sequencing data using R and Bioconductor. *Nat. Protoc.* **8**, 1765–1786 (2013).
64. Rendeiro, A. F. et al. Chromatin accessibility maps of chronic lymphocytic leukaemia identify subtype-specific epigenome signatures and transcription regulatory networks. *Nat. Commun.* **7**, 11938 (2016).
65. Jiang, H., Lei, R., Ding, S. W. & Zhu, S. Skewer: a fast and accurate adapter trimmer for next-generation sequencing paired-end reads. *BMC Bioinforma.* **15**, 182 (2014).
66. Tarasov, A., Vilella, A. J., Cuppen, E., Nijman, I. J. & Prins, P. Sambamba: fast processing of NGS alignment formats. *Bioinformatics* **31**, 2032–2034 (2015).
67. Consortium, E. P. An integrated encyclopedia of DNA elements in the human genome. *Nature* **489**, 57–74 (2012).
68. de Hoon, M. J., Imoto, S., Nolan, J. & Miyano, S. Open source clustering software. *Bioinformatics* **20**, 1453–1454 (2004).

69. Saldanha, A. J. Java Treeview—extensible visualization of microarray data. *Bioinformatics* **20**, 3246–3248 (2004).

Acknowledgements

We thank Alexander Rudensky (Memorial Sloan-Kettering Cancer Center) for providing mice, Frank Lyko for help with amplicon sequencing, Claudia Schmitt, Ulrike Rothermel, Sabine Schmitt, Anna von Landenberg, Kristin Lobbes (all DKFZ), Marina Wuttke, Brigitte Ruhland, Veronika Hofmann, Kathrin Schambeck, Luise Eder, Rudolf Jung (all University Regensburg) and Marie-Luise Brunn (BNITM Hamburg) for excellent technical support. Furthermore, we thank the DKFZ core facilities for preclinical research, microscopy, flow cytometry and genomics & proteomics for outstanding support. This work was supported by grants from the Helmholtz Association of German Research Centers (HZ-NG-505) and the European Research Council (ERC-CoG, #648145 REGIREG) and the Deutsche Forschungsgemeinschaft (DFG, German Research Foundation- Projektnummer 324392634-TRR 221) to M.F., M.D. was supported by the German–Israeli Helmholtz Research School in Cancer Biology.

Author contributions

M.D., M.B., J.A. and M.F. designed experiments; M.D., Y.H., W.H., F.B., D.K., U.T., A.-C. H., S.B., D.W., A.B. and G.F. performed the experiments; R.M.S. provided material; M.D., C.S., M.B., W.H., C.I., A. H.-W., T.H., H.J.G., M.R., J.A. and M.F. analyzed data; M.D. and M.F. wrote the manuscript.

Additional information

Supplementary Information accompanies this paper at <https://doi.org/10.1038/s41467-019-09276-w>.

Competing interests: The authors declare no competing interests.

Reprints and permission information is available online at <http://npg.nature.com/reprintsandpermissions/>

Journal peer review information: *Nature Communications* thanks Derk Amsen and the other anonymous reviewer(s) for their contribution to the peer review of this work. Peer reviewer reports are available.

Publisher's note: Springer Nature remains neutral with regard to jurisdictional claims in published maps and institutional affiliations.



Open Access This article is licensed under a Creative Commons Attribution 4.0 International License, which permits use, sharing, adaptation, distribution and reproduction in any medium or format, as long as you give appropriate credit to the original author(s) and the source, provide a link to the Creative Commons license, and indicate if changes were made. The images or other third party material in this article are included in the article's Creative Commons license, unless indicated otherwise in a credit line to the material. If material is not included in the article's Creative Commons license and your intended use is not permitted by statutory regulation or exceeds the permitted use, you will need to obtain permission directly from the copyright holder. To view a copy of this license, visit <http://creativecommons.org/licenses/by/4.0/>.

© The Author(s) 2019